ISTANBUL TECHNICAL UNIVERSITY ★ GRADUATE SCHOOL OF SCIENCE ENGINEERING AND TECHNOLOGY

VIBRO-ACOUSTIC ANALYSIS OF A REFRIGERATOR FREEZER CABINET COUPLED WITH THE AIR DUCT

M.Sc. THESIS

Onur ÇELİKKAN

Department of Mechanical Engineering

System Dynamics and Control Program

May 2014

ISTANBUL TECHNICAL UNIVERSITY ★ GRADUATE SCHOOL OF SCIENCE ENGINEERING AND TECHNOLOGY

VIBRO-ACOUSTIC ANALYSIS OF A REFRIGERATOR FREEZER CABINET COUPLED WITH THE AIR DUCT

M.Sc. THESIS

Onur ÇELİKKAN
(503071622)

Department of Mechanical Engineering

System Dynamics and Control Program

Thesis Advisor: Prof. Dr. Haluk EROL

May 2014

İSTANBUL TEKNİK ÜNİVERSİTESİ ★ FEN BİLİMLERİ ENSTİTÜSÜ

BUZDOLABI DONDURUCU BÖLMESİNİN HAVA KANALI İLE BİRLİKTE AKUSTİĞİNİN İNCELENMESİ

YÜKSEK LİSANS TEZİ

Onur ÇELİKKAN
(503071622)

Makina Mühendisliği Anabilim Dalı

Sistem Dinamiği ve Kontrol Programı

Tez Danışmanı: Prof. Dr. Haluk EROL

MAYIS 2014

Onur ÇELİKKAN, a M.Sc. student of ITU Graduate School of Science Engineering and Technology, student ID 503071622, successfully defended the thesis entitled "VIBRO-ACOUSTIC ANALYSIS OF A REFRIGERATOR FREEZER CABINET COUPLED WITH THE AIR DUCT", which he prepared after fulfilling the requirements specified in the associated legislations, before the jury whose signatures are below.

Thesis Advisor :	**Prof. Dr. Haluk EROL** İstanbul Technical University	....
Jury Members :	**Assoc. Prof. Dr. İ. Murat KOÇ** İstanbul Technical University	....
	Assist. Prof. Dr. Çetin YILMAZ Boğaziçi University	....

Date of Submission : 5 May 2014
Date of Defense : 30 May 2014

FOREWORD

I would like to express my deepest gratitude to my advisor, Professor Haluk EROL, for giving me the opportunity to work on this project and for his support, guidance and suggestions. It is a pleasure and honor being his student.

Specifically I wish to thank Mr. H. Emrah ŞAFAK for their help, for providing the experimental data and for making a nice atmosphere at the work.

Finally, it’s my deepest pride to thank here Gamze ÇELİKKAN and my family. My journey has been their journey and this thesis is dedicated to their love.

May 2014 Onur ÇELİKKAN
(NVH Engineer)

TABLE OF CONTENTS

Page

ABBREVIATONS

AFSI	**:**	Acoustic Fluid Structure Interaction
ASI	**:**	Acoustic Structure Interaction
BEM	**:**	Boundary Element Method
BLDC	**:**	Brushless Direct Current
CFD	**:**	Computational Fluid Dynamics
FEM	**:**	Finite Element Method
FFT	**:**	Fast Fourier Transform
FRF	**:**	Frequency Response Function
FSI	**:**	Fluid Structure Interaction
MMA	**:**	Method of Moving Asymptotes
SST	**:**	Shear Stress Transport

LIST OF TABLES

Page

LIST OF FIGURES

Page

VIBRO-ACOUSTIC ANALYSIS OF A REFRIGERATOR FREEZER CABINET COUPLED WITH THE AIR DUCT

ABSTRACT

The number of complaints about noise in living environments is rapidly increasing; specifically, there are concerns about noise from household electric appliances. Unlike other home appliances, refrigerators operate all day, and users respond sensitively to the noise they generate. Therefore, in order to create quieter living environment, it is necessary to reduce the sound pressure levels of refrigerators.

Together with the compressor, the fan is a source of noise that contributes the most to the refrigerator's overall noise level. Fans in refrigerators are used for several purposes: for cooling the compressor, for circulating cold air from the evaporator to the freezer and the cool chamber, and for making ice for the ice dispenser. In large refrigerators, what is needed to rotate circulating fan faster to generate larger flowrates. Such high-speed rotation causes fan noise to be of greater concern than other sources of noise in a refrigerator.

With the improvement in computational technology, systematic design tools which are used to estimate the noise generation mechanism of fans and the interaction with the coupled structures become essential in creating low-noise designs. Experimental techniques involve some difficulties including time and investment expenses to build measurement environment. Because of these difficulties computational methods become one of the commonly selected techniques in development process.

In this thesis, vibro-acoustic interaction between the structure and cavity inside the freezer cabinet was investigated. For this purpose, a set of numerical and experimental analyses were performed. In numerical analyses, acoustic characteristic of the freezer cavity was solved and then the mixed finite element method was implemented to analyze the coupled behavior of the cavity with air duct by using Acoustic Fluid-Structure Interaction (AFSI) technique. In experimental analyses, acoustic modal analysis of the freezer cavity and structural modal analysis of the air duct were performed for validation process. A good agreement was obtained among the results. Thus also the accuracy of the numerical model was confirmed.

The validated models were used for the design optimization. For solving the noise generation mechanism inside the freezer cabinet primarily the noise generated by the freezer fan unit was measured in normal working condition of the refrigerator and the resonance frequencies was obtained. This information was compared with the normal modes of the air duct thereby the overlapping frequencies was identified. In order to reduce the interaction between the source and the structure some design modifications were applied to the air duct. So the structural borne noise which is radiated from the air duct into the freezer cavity was reduced.

BUZDOLABI DONDURUCU BÖLMESİNİN HAVA KANALI İLE BİRLİKTE AKUSTİĞİNİN İNCELENMESİ

ÖZET

Yaşam alanlarında, çevresel kaynaklı gürültüden şikayet eden insan sayısı günümüzde hızla artmaktadır, özellikle elektrikli ev aletlerinden yayılan gürültünün bu duruma büyük bir katkısı vardır. Diğer elektrikli ev aletlerinden farklı olarak, buzdolapları durmaksızın sürekli olarak çalışırlar, bu durumda buzdolaplarını daimi bir gürültü kaynağı haline getirir ve yaşam alanlarında yüksek gürültülü ve sürekli ses alanlarının oluşmasına sebep olur. Bu yüzden kullanıcılar buzdolaplarının yaydığı gürültüye karşı daha hassaslardır. Sessiz bir yaşam alanı yaratmak için buzdolaplarından yayılan gürültünün azaltılması gerekmektedir.

Kompresör ile birlikte fan, buzdolabının yaydığı toplam gürültüye en çok katkısı olan gürültü kaynaklarıdır. Buzdolaplarında fanlar: kompresörü soğutmak için, evaporatörden geçen soğuk havayı dondurucu ve soğutucu bölmeler arasında dolaştırmak için ve buz dispanserinde buz yapmak için kullanılırlar. Büyük hacimli buzdolaplarında gerekli soğuk hava debisini sağlayabilmek için daha yüksek devirlerde çalışan fanlara ihtiyaç duyulur. Bu gibi durumlar fanların daha fazla gürültü üretmesine ve buzdolaplarından yayılan gürültüye daha çok katkıda bulunmalarına sebep olur.

Sayısal hesaplama teknolojilerinde ki gelişmeler ile birlikte, fan kaynaklı gürültü oluşumunu ve bu gürültünün diğer yapılar ile olan etkileşimlerini kestirmek için kullanılan sistematik analiz yöntemleri düşük gürültülü tasarımlar oluşturmak için zorunlu bir kıstas haline geldiler. Özellikle deneysel analiz tekniklerinin gerçekleştirilmesi için gereken zaman ve yatırım harcamaları göz önünde bulundurulduğunda, geliştirme sürecinde sayısal hesaplama yöntemlerinin önemi daha çok anlaşılmaktadır.

Bu tezde, buzdolabı dondurucu bölmesini oluşturan yapı ile kavite arasında ki titreşim akustiği etkileşimi ve bu etkileşimin gürültü üretimine katkısı incelendi. Bu amaçla bir takım sayısal ve deneysel analizler gerçekleştirildi.

Sayısal analizler iki aşamada gerçekleştirildi. İlk aşamada buzdolabı dondurucu bölmesini oluşturan komponentler ayrı ayrı ele alınarak değerlendirildi. Buzdolabı dondurucu bölmesini oluşturan kavite sayısal olarak modellenerek, sonlu elemanlar metodunun kullanılması ve akustik modal analiz yöntemi ile kavitenin akustik doğal frekansı ve bu frekanslara ait mode şekilleri hesaplandı. Kaviteyi oluşturan hacmin, basit geometrik bir forma sahip olmasından dolayı elde edilen sonuçlar formülasyonlar ile analitik olarak da hesaplanarak modelin doğruluğu kanıtlanmıştır. Akustik kavitenin analizine ek olarak, buzdolabı dondurucu bölmesinde yapıyı oluşturan hava kanalının da modal analizleri gerçekleştirildi. Hava kanalını oluşturan kanal ve kapak parçaları ayrı ayrı modellenerek, her iki yapının doğal frekansları ve bu frekanslara ait mode şekilleri elde edilmiştir.

İkinci aşamada gerçeğe daha yakın bir model oluşturmak amacı ile buzdolabı dondurucu bölmesini oluşturan yapılar, bir arada ele alınarak, yapıların montajlanmış

halde gösterdiği davranışlar incelenmiştir. Buna ek olarak buzdolabı dondurucu bölmesinde, hava kanalının arkasında yer alan ve dondurucu ile soğutucu arasındaki soğuk hava akışını sağlayan eksenel fanda modellenerek, akışın yapılar üzerinde yarattığı statik basıncın yine yapıların davranışları üzerindeki etkisi de göz önünde bulundurulmuştur.

Hava kanalı içindeki akış alanını çözümlemek amacı ile fan ile birlikte akış alanını oluşturan hava kanalı iç hacmi modellenmiştir. Fan kaynaklı akış, kayma gerilimi taşıma (KGT) türbülans yöntemi kullanılarak çözdürülmüştür. Hava kanalı üzerindeki giriş ve çıkış delikleri tanımlanarak, sınır koşulları oluşturulmuştur. Hareketli referans çerçeve metodu kullanılarak fan kanatlarının sanal olarak fan devrine uygun olarak dönmesi sağlanmıştır. Akış alanını oluşturan yapı ile hava kanalını oluşturan yapı akışkan-yapı etkileşimi tekniği ile birleştirilerek, akış kaynaklı basınç dağılımı tek yönlü eşleme metodu ile hava kanalına aktarılmıştır. Hava kanalında basınç kaynaklı kuvvetler, yapısal statik analizde ön gerilim olarak tanımlanarak yapının deformasyonu hesaplanmıştır. Akustik-yapı etkileşimi tekniği ile öngerilimli hava kanalı kapağı ile dondurucu kavite modeli eşleştirilerek, oluşan sistemin bir arada gösterdiği davranışı incelemek amacı ile frekans domaininde modal analizler gerçekleştirilmiş ve yapıların bir arada iken ki doğal frekansları ve mode şekillerindeki değişim ortaya çıkarılmıştır.

Oluşturulan sayısal modeli doğrulamak amacı ile çalışma konusu olan ürün üzerinde deneysel analizler gerçekleştirildi. Deneysel akustik modal analiz yöntemi kullanılarak, dondurucu hacmin akustik doğal frekansları elde edildi. Bu yöntemde hava kanalı içinde fanın bulunduğu konuma bir düşük frekans hoparlörü yerleştirilerek, yapının akustik olarak tahrik edilmesi sağlandı. Bir sinyal üreteci kullanılarak hoparlörden 0 ile 1250 Hz arasında beyaz gürültü verildi. Bu şekilde hem hava kanalı tarafından üretilen yapısal kaynaklı gürültünün hem de dondurucu kavitenin akustik doğal frekanslarının tahrik edilmesi sağlandı. Buzdolabı dondurucu bölmesine iki adet mikrofon yerleştirilerek, frekans cevabı fonksiyonu ölçüldü. Kullanılan mikrofonlardan biri hoparlörün önüne yerleştirilerek kaynağın ürettiği ses basıncını ve frekansını ölçmek amacı ile referans mikrofon olarak kullanıldı. Bir diğeri de dondurucu hacim içine yerleştirilerek kavite içinde ki basınç dağılımını ölçmek için cevap mikrofonu olarak kullanıldı. Bu şekilde 12 noktadan veri toplanarak dondurucu kavitenin akustik modal analizi gerçekleştirildi. Tüm ölçümler oda sıcaklığındaki yarı yankısız akustik odada alındı.

Hava kanalını oluşturan kanal ve kapak parçalarının kavite içinde ölçülen düşük frekanslarda ki rezonans frekanslarına olan katkısını görmek amacı ile her iki yapının da darbe çekici kullanılarak deneysel modal analizleri gerçekleştirildi. Bu şekilde yapıların doğal frekansları ile birlikte modal animasyon tekniği ile bu frekanslarda gösterdikleri mode şekilleri elde edildi.

Değerlendirme bölümünde kaviteye ve yapılara ait sayısal ve deneysel analizler bir araya getirilerek, doğal frekansları ve mode şekilleri kıyaslandı. Sonuçlar arasında iyi bir uyum elde edilerek, sayısal modellerin doğruluğu kanıtlandı.

Doğrulanmış modeller tasarım optimizasyonu için kullanıldı. Dondurucu kabin içinde gerçekleşen gürültü üretim mekanizmasını çözmeye yönelik olarak buzdolabının normal çalışma koşulları altında, dondurucu fan motoru tarafından üretilen gürültü ölçüldü ve rezonans frekansları tespit edildi. Bu frekanslar, hava kanalının kendi doğal frekansları ile kıyaslanarak birbirleri ile çakışan frekanslar tespit edildi. Kaynak ile yapı arasında ki bu frekans etkileşimini indirgemek amacı ile hava kanalına bazı tasarımsal değişiklikler uygulandı. Böylece hava kanalından kaviteye yayılan gürültünün azaltılması sağlandı.

1. INTRODUCTION

1.1 Literature

Sound comfort is among the most important design criteria in a variety of technical fields and a challenging task in industrial applications. The rapidly growing technologies make possible to produce more efficient, ecologic and silent products. These new developed technologies also increase the expectations of consumers to low noise products. Besides that, the noise emission levels become the distinctive feature between the products which compete at the same market. The increasing awareness on the effect of noise on human health and the resulting strict governmental regulations concerning the noise emission enforce designers to focus on noise reduction more than ever.

The most frequently encountered noise sources in natural living environment of consumers are the household appliances in residential areas. Especially the refrigerators are the main sources of this product family, cause of the continuous working principle that creates noisy sound field. Therefore, reduction in noise from a refrigerator is necessary and noise-free operation is becoming the preferred choice of consumers in the domestic refrigerators.

Many older-type refrigerators with static cooling system are equipped with one or more compressors so the main sources of noise are compressors and circulating refrigerant. However, nowadays new technologies constantly being introduced to market to improve refrigerator users' comfort. One of the modern solutions is the no-frost (or frost free) type of refrigerator which uses an auto-defrost technique which regularly defrosts the evaporator in a refrigerator or freezer. This type of refrigerators are equipped in an additional ventilation fan mounted in air duct to circulate the cooled air and to aid in the defrosting process. In this type of configuration, the fan together with the compressor becomes a source of noise that contributes the most to the overall noise level of the refrigerator and also increases the vibration and the resulting sound level a few decibels in comparison with static cooling refrigerator.

Furthermore, increasing in demand of the more fresh-food storage causes refrigerators to have larger volumes which need to faster ventilation fans to generate larger flow rates. Such high-speed rotation causes generating more sound energy and this situation increase the priority of the fan among the other noise sources in refrigerator.

This case shows that applying new technologies in refrigerators' construction involves additional noise and vibration sources which need to be investigated. Noise reduction in refrigerators was widely studied by various institutions but research on ventilation fan noise is rather slight.

Baran et al. (2009) observed that the main source of vibration typical for the no-frost refrigerator is the unbalance of the blades of the ventilation fan which stimulates the plenum and effectively the whole structure to vibrate. The analysis results show that a good indicator of the unbalance is the change of frequency and vibration level of the fundamental component of rotation. The experimental investigation demonstrated that unbalance may cause a substantial increase of vibration level and higher noise levels.

The next step of the investigation is the structure borne noise caused by vibration of the plenum. The measurements indicated that vibration frequencies were obtained at harmonics of the rotational speed of the fan and caused by the magnetic force produced by the motor coil. These results show that the maximum vibration levels for all frequencies occurs at the plenum cover, where the ventilation fan is mounted. It proved that the ventilation fan is the main source of the vibration.

Seo et al. (2000) achieved reduction on refrigerator's sound pressure level by isolating the transmission of ventilation noise between the freezer compartment and machinery room.

Takushima et al. (1992) investigated the flow characteristic which leaves from blade surface and clearly found that the flow through the impeller was not symmetrical to the axis. They showed that the unsymmetrical flow is caused by the restriction of flow passages, and this produce the impeller noise. They performed some design changes on blades to prevent the flow from unsymmetry. Besides, Takushima et al. (1992) searched for the sound sources by the sound intensity method indicated that the noise was radiated through the openings of the front board. They installed the guiders on the rear board in the fan unit to guide the flow away from the openings. As a result, the impeller noise was reduced, whereas the flow was kept almost the same.

Igarashi et al. (2002) performed CFD (Computational Fluid Dynamics) analyses by evaluating the flow fields of a propeller fan used in a freezing compartment of household refrigerators. They designed not only propeller fans but also flow ducts to reduce fan noise because the high pressure resistance of the complex shaped duct where the fan is located. By changing the shape of a bell mouth and width of upstream duct, they successfully improved flow characteristics to achieve large noise reduction.

Kim et al. (2006) identified the source of excessive noise in the small fan-motor system for household refrigerators. They investigated an undesirable effect of cogging torque from BLDC motor that prevents the smooth rotation of the rotor and result in noise. Cogging torque arises from the saliency of the slot structure for winding, and depends on the magnetization pattern of the permanent magnet and the shape of the core (Tajima et al, 1987). The results were showed that the source is a mechanical resonance excited by torque ripple of the BLDC motor.

Gue et al. (2011) carried out experimental and numerical investigations on the aerodynamic noise of axial fan to develop a low noise fan, which is used to cool a compressor and a condenser in the mechanical room in a household refrigerator. First, they experimentally investigated the noise performance of the target fan and then applied computational aeroacoustic techniques based on the hybrid method to predict the radiated sound pressure levels. In this method, first, the flow information is predicted by analysis tools such as computational fluid dynamics (CFD), and second, the acoustic field is predicted by using the flow field information with an acoustic modeling, which is based on Lighthill's acoustic analogy (Lighthill, 1952). The validity of the computational aeroacoustic techniques was confirmed by comparing the predictions with the measurements. To develop a low-noise fan, they created two design concepts: one was that the uneven grooves are made on the surface of the suction side of blade along the rotational direction, and the other is that two different blades are combined into one blade. By applying the proposed design factors to the existing fan in household refrigerator, the results showed that the overall noise from the new fan is reduced by approximately 1dB to 2.2 dB in comparison with that from existing fan.

Fan noise involves both tonal and broad band components: Tonal noise due to blade passing frequency and broad band due to turbulent fluctuations and the interaction with casing resonance caused by excitation of a natural acoustic frequency. For fan noise generation, the source mechanism of which may be categorized according to the types of fan: centrifugal fan and axial fan. To centrifugal fans, many researchers have shown that the main source of aerodynamic tonal noise generation is the interaction between the non-uniform impeller flow and the fixed tongue (Neise, 1976, 1982, in pres). Velarde-Suarez (2006) carried out an experimental study on the source of tonal noise from centrifugal fans. They showed that strong source of noise at the blade-passing frequency (BPF) is the interaction between the fluctuating flow that leaves the impeller and the volute tongue, and that the source region is concentrated in the vicinity of volute tongue. Based on this finding, Velarde-Suarez (2008) performed experiments on the reduction of aerodynamic tonal noise of centrifugal fans by modifying the volute tongue. For axial fans, the dipolar force over the surface of blades is recognized as the main contribution to overall noise (Gerard et al, 2005). Recently, Heo and Cheong (2011) developed low-noise centrifugal fans by modifying the linear trailing edge lines of the fan blades into inclined S-shaped lines. Although there have been many researches on axial fan noise, there is no generally accepted low-noise fan.

Numerical fan noise prediction usually investigates tonal and broadband noise separately. The studies of Gutin are considered as the pioneer work about the acoustics of axial flow machinery, which were published in the late 40's (Sorgüven, 2004). Recently, Carolus (2003) and Bommes et al. (2003) have made notable contributions about the aerodynamics and the acoustics of the fans.

Marretta et al. (2001) implemented k-ε method for obtaining the unsteady characteristics of a realistic turbulent flow interacting with rectangular flat plate undergoing "ground effect".

Lee et al. (2010) studied to compute the internal blade-passing frequency (BPF) noise of a centrifugal fan in a household refrigerator by using a hybrid method. They predicted the unsteady flow field of the centrifugal fan in a duct by solving the incompressible Reynolds-Averaged Navier-Stokes (RANS) equations with conventional computational fluid dynamic techniques and then the principal sources of noise were extracted from the predicted flow field through the acoustic analogy.

Maaloum et al. (2004) investigated the aeroacoustic performance of axial flow fans based on the unsteady pressure field on blade surface. First, the unsteady aerodynamic forces applied on the fan blades were evaluated by using aerodynamic approach based on the vortex surface method. They found that the sources of noise corresponding to the zones with high force fluctuation amplitude were located initially on the blade surface. Then, these fluctuating forces were used to predict the tonal noise radiated by the fan in the far field by means of the Ffowcs Williams and Hawkings (FW-H) equation.

In order to simulate the acoustic-structure interaction (ASI) between the structure and the acoustic cavity, it is required to be solved the coupled field equations using the fluid-structure interaction algorithms. In many engineering fields, dynamic response in fluid-structure interaction (FSI) is very important, and some of the FSI phenomena are treated as an acoustic FSI (AFSI) problem. The dynamic interaction between fluids and structures may change the dynamic characteristics of the structure and its response to external sources of excitation. In addition, interaction among structures occurs when they are closely spaced and immersed in fluid. Such an interaction must be carefully considered when designing structures, especially when high accuracy is required.

The acoustic pressure computation often requires modeling of both the structure that generates the acoustic pressure wave and the fluid medium that transmits the wave. Zienkiewicz and Newton (1969) first presented the finite element (FE) discretization of the acoustic wave equation to solve this fluid-structure interaction problem. When a structure is in contact with fluid medium, the formulation is effectively applied to predict the acoustic pressure and the structural displacement response to harmonic excitations induced in either or both the parts of the coupled problem.

Rajakumar et al. (1990) studied in 2-D fluid-structure interaction problems and formulated an acoustic coupling element capable of coupling the boundary element (BE) and finite element (FE) discretization. The Helmholtz equation governing the acoustic pressure in a fluid was discretized using the BE method and coupled to the

FE discretization of a vibrating structure that is contact with the fluid. They also validated the coupled element by verifying the computed results of a simple problem whose theoretical solution is known.

Mathews (1986) described two ways of solving the coupled acoustic BE – Structural FE problems. One of the methods called the structural variable methodology requires the elimination of the unknown surface pressures at the fluid-structure interface to cast the coupled equations in terms of the unknown structural displacements. The second method, namely the fluid variable methodology, involves the elimination of the structural displacements to get an equation in terms of the unknown pressures. These two procedures involve two step computations in order to get the complete solution to the fluid-structure interaction problem. In the structural variable method, the fluid pressures will have to be computed by substituting the displacement solution in the acoustic BE equation, and vice versa in the fluid variable method.

Fischer and Gaul (2006) used to fast multipole BEM method to solve a large-scale simulations of acoustic-structure interaction problems. They adapted the mortar method proposed by Bernardi et al. (1994) to BEM-FEM coupling algorithm on the coupled interface that allows the combination of non-conforming meshes. Instead of the using classical BEM-FEM coupling approaches that quadratically increasing computing time and memory requirements with the number of boundary elements, the fast multipole algorithm was used to reduce the numerical cost for the evaluation of the BEM matrix-vector product to quasi-linear. This large savings of the fast multipole BEM were achieved by series expansion of the fundamental solution and a hierarchical multi-level scheme.

Minami et al. (2014) studied on the large-scale acoustic fluid-structure interaction problem to determine the dynamic response of tube bundles inside the fluid domain. They used a parallel iterative partitioned coupling algorithm to attain robust and fast convergence of fixed-point iterations on coupled interface. This method improves accuracy and robustness compared with a monolithic method. In the iterative partitioned method, fluid and structural problems are solved separately and iteratively until conditions related to equilibrium and geometrical compatibility are satisfied. They also implemented experimental analyses and the numerical results showed good agreement with experimental results.

Akl et al. (2009) developed a mathematical model of a plate coupled with an acoustic cavity to simulate fluid-structure interactions based on the theory of finite elements method. They used a topology optimization approach which utilizes the moving asymptotes method to minimize the fluid-structure interactions at different structural frequencies. The method of moving asymptotes (MMA), (Svanberg, 1987, 1999, in pres) was developed to minimize the coupling between the flexible plate and the acoustic domain. So, the energy transfer between the two domains was minimized and consequently the natural frequencies of the fluid-loaded structure were affected. The obtained results demonstrate the effectiveness of the proposed approach in simultaneously attenuating the structural vibration and the sound pressure inside the acoustic domain at several structural frequencies by proper redistribution of the plate material. The presented approach also created an invaluable tool in the design of a wide variety of critical structures which must operate quietly when subjected to fluid loading.

Jensen et al. (2006) performed topology optimization of a coupled acoustic-structure system by adopting the mixed finite element procedure called a *u/p-formulation* with the displacement field and the pressure as primal variables. They modified the governing equations, Helmholtz equation (Wave equation) for acoustic cavity and the linear elasticity equation for structure, and imposed the coupling boundary conditions at the boundary layer to optimize coupled system by using the shape optimization scheme. This mixed formulation made possible to analyze the displacement and the response of a compressible media in the single governing equation.

The goal of this study is to analyze the acoustic characteristic of the freezer compartment coupled with the air duct. For this purpose, the study divided to two section, at one section fluid analyses has been performed with fan blade in air duct and pressure distribution was solved on the interior surfaces of the fan louver and evaporator cover and at second section coupled acoustic modal analyses has been performed between the air duct and the freezer compartment by using the acoustic-structure interaction techniques. All numerical models were created with ANSYS Workbench R15.0 finite element analysis and simulation software. The results were obtained from numerical solutions have been validated by experimental results. In validation process, experimental modal analysis was performed for the air duct and the experimental acoustic modal analysis was performed for the freezer compartment using external sound source. As a consequence, vibration characteristic of the air duct resolved and the contribution to the noise generation in freezer compartment has been observed.

2. THEORY AND PRINCIPLES

2.1 Theory of Computational Fluid Dynamics

For computation of fluid-structure interaction, boundary layer has to be resolved with high accuracy to determine the pressure fluctuations over the surface of a fan blade and an air duct. Navier-Stokes equations are adequate to describe the time-dependent behavior of three regimes, namely laminar, transitional and turbulent generally noticed in a flow field. The Navier-Stokes equations consist of three fundamental equations: conservation of mass, conservation of momentum and conservation of energy. They are expressed in a conservative form in a Cartesian coordinate system as:

$$\frac{\partial}{\partial t}\begin{pmatrix}\rho \\ \rho\vec{v} \\ \rho E\end{pmatrix} + \vec{\nabla}.\begin{pmatrix}\rho\vec{v} \\ \rho\vec{v}\otimes\vec{v} + pI - \tau \\ \rho\vec{v}H - \tau\cdot\vec{v} - K\nabla T\end{pmatrix} = \begin{pmatrix}0 \\ \rho\vec{f_e} \\ W_f + q_H\end{pmatrix} \quad \textbf{(2.1)}$$

Where ρ is the density, $\vec{v}$ is the velocity vector, E is the internal energy, H is the enthalpy, p is the pressure, $\boldsymbol{\tau}$ is the stress tensor, I is the identity matrix, K is the thermal conductivity of the fluid and q_H represents the contribution of heat sources. f_e represents external forces, with W_f being the work done by external forces, $W_f = \rho\overrightarrow{f_e}\cdot\vec{v}$. The coefficients of the stress tensor, $\boldsymbol{\tau}$ for Newtonian fluids are given by

$$\tau_{ij} = \mu(T,p)\left[\left(\partial_i v_j + \partial_j v_i\right) - \tfrac{2}{3}\left(\vec{\nabla}\cdot\vec{v}\right)\delta_{ij}\right] \quad \textbf{(2.2)}$$

Where μ is the absolute viscosity of the fluid and δ_{ij} is the delta function which is one on the diagonal and is zero elsewhere.

Assuming the sources are known, we have unknown thermodynamic variables ρ, u, v, w, p, s and h or e. h and e are functions of two of the other variables (p and T). This can be shown by rewriting the energy equation as an equation for internal energy,

$$\rho\frac{\partial e}{\partial t} = -p\left(\vec{\nabla}\cdot\vec{v}\right) + \vec{\nabla}\cdot(K\nabla T) + \varepsilon_v + q_H \quad \textbf{(2.3)}$$

Or static enthalpy (h),

$$\rho \frac{\partial h}{\partial t} = \frac{dp}{dt} + \vec{\nabla} \cdot (K \nabla T) + \varepsilon_v + q_H \quad \textbf{(2.4)}$$

Where ε_v is the dissipation term,

$$\varepsilon_v = (\tau \cdot \nabla) \cdot \vec{v} \quad \textbf{(2.5)}$$

We can then remove e and h from the energy equation by applying one of the relationships,

$$de = c_v dT \text{ or } dh = c_p dT \quad \textbf{(2.6)}$$

To Eqs. (2.3) or (2.4). c_v and c_p are the specific heats of the fluid at constant volume and pressure, respectively. By assuming a perfect gas, we gain an additional equation, the equation of state:

$$p = \rho R T \quad \textbf{(2.7)}$$

We now have six equations and six unknowns. The entropy is de-coupled and can be found independently of the flow solution from basic thermodynamics:

$$T ds = dh - \frac{dp}{\rho} \quad \textbf{(2.8)}$$

2.1.1 Turbulence model

Three different regimes, namely laminar, transitional and turbulent, can generally be noticed in a flow field. In turbulent flows, the time-averaged flow parameters fluctuate in all three spatial dimensions. Due to the instability of the laminar state, flow changes from laminar to turbulent, with the amplified small disturbances. After the rotational flow structures are developed, the turbulent kinetic energy is transferred from larger eddies to smaller ones, with the smallest eddies eventually dissipating into heat through molecular viscosity.

A non-dimensional parameter for flow behavior is the Reynolds number:

$$Re = \frac{UL}{v} \quad \textbf{(2.9)}$$

Where and U and L are characteristic velocity and length scales of the mean flow and v is the kinematic viscosity of the fluid. According to Reynolds number, turbulence occurs when the convection is much stronger than the dissipation.

A turbulent flow field at high Reynolds number consists of vortices (eddies) of various sizes, from the largest to the smallest ones. Each eddy can be related to a scale of velocity, time and length. These initial large vortical scales will break up due to vortex stretching to develop smaller and smaller scale structures.

The different length scales are often referred to a turbulent flow field: i) the integral length scale (l), ii) Taylor microscale (λ) and iii) Kolmogorov microscale (η).

The largest scales of turbulence can be estimated by the integral length scale. This represents the mean distance for which the velocity fluctuations are correlated. The integral scales, often referred to as energy-bearing eddies, is related to ε, so that

$$\eta/l \sim Re_T^{-3/4} \qquad \textbf{(2.10)}$$

Where $Re_T = k^{1/2}l/v$ is the usual turbulence Reynolds number. Since values of Re_T greater of 10^4 are typical of fully developed turbulent boundary layers and $l \sim 0.1\delta$ where δ is boundary-layer thickness.

For isotropic turbulence, Taylor microscale is defined by

$$\varepsilon = 15v\overline{\left(\frac{\partial u'}{\partial x}\right)^2} \equiv 15v\frac{\overline{(u')^2}}{\lambda^2} \qquad \textbf{(2.11)}$$

The smallest scales in turbulence are the Kolmogrov scales. Kolmogrov scales of length, time and velocity are

$$\eta \equiv (v^3/\varepsilon)^{1/4} \quad \tau \equiv (v/\varepsilon)^{1/2} \quad v \equiv (v\varepsilon)^{1/4} \qquad \textbf{(2.12)}$$

Kolmogorov length scale, (η) outside the viscous wall region is less than 1/1000 times the thickness of the boundary layer.

As shown in Fig. 2.1 three distinct regions of turbulent eddies can be identified, namely the energy containing eddies, the inertial subrange and the dissipation subrange. The integral scale, which is determined by the geometry of the flow, contains most of the turbulent kinetic energy. This energy is continuously supplied by the mean flow. Taylor microscale is in the inertial subrange and is much smaller than the integral scale but it is much larger than the Kolmogorov microscale. Turbulence scales that are part of the inertial subrange receive energy from the larger scales of turbulence and subsequently they lose energy by transferring it to the smaller scales. This process is named "*the energy cascade*". The smallest length scales (Kolmogorov) in the energy spectrum are in the dissipation subrange. At this level the viscosity is important and the entire kinetic energy of eddies is transferred into heat by viscous dissipation.

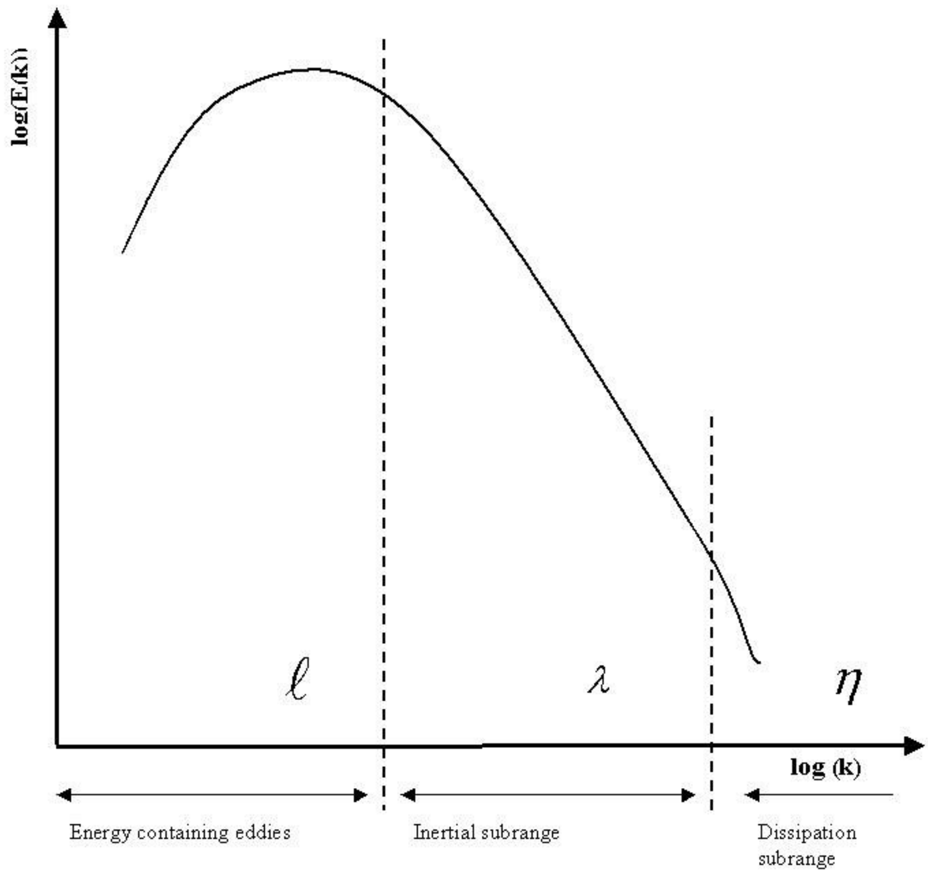

Figure 2.1 : Turbulent kinetic energy spectrum.

In this study, the turbulence transport, turbulence production and turbulence dissipation are modeled by the transitional SST turbulence model. This model is a hybrid two-equation model that combines the advantages of both $k - \epsilon$ and $k - \omega$ models.

2.1.1.1 Translational shear stress turbulence model

The transition SST model is based on the coupling of the $k - \omega$ transport equation with two other transport equations, one for the intermittency and one for the transition onset criteria, in terms of momentum-thickness Reynolds number.

The transport equation for the intermittency γ is defined as:

$$\frac{\partial(\rho\gamma)}{\partial t} + \frac{\partial(\rho U_j \gamma)}{\partial x} = P_{\gamma 1} - E_{\gamma 1} + P_{\gamma 2} - E_{\gamma 2} + \frac{\partial y}{\partial x_j}\left[\left(\mu + \frac{\mu_t}{\sigma_\gamma}\right)\frac{\partial y}{\partial x_j}\right] \qquad \textbf{(2.13)}$$

The transition sources are defined as follows:

$$P_{\gamma 1} = C_{a1} F_{length} \rho S [\gamma F_{onset}]^{C_{\gamma 3}} \qquad \textbf{(2.14)}$$

$$E_{\gamma 1} = C_{e1} P_{\gamma 1} \gamma \qquad \textbf{(2.15)}$$

Where S is the strain rate magnitude, F_{length} is an empirical correlation that controls the length of the transition region and C_{a1} and C_{e1}hold the values of *2* and *1*, respectively. The destruction/relaminarization sources are defined as follows:

$$P_{\gamma 2} = C_{a2} \rho \Omega \gamma F_{turb} \qquad \textbf{(2.16)}$$

$$E_{\gamma 2} = C_{e2} P_{\gamma 2} \gamma \qquad \textbf{(2.17)}$$

Where Ω is the vorticity magnitude. The transition onset is controlled by the following functions:

$$Re_V = \frac{\rho y^2 S}{\mu} \qquad \textbf{(2.18)}$$

$$R_T = \frac{\rho k}{\mu \omega} \qquad \textbf{(2.19)}$$

$$F_{onset1} = \frac{Re_V}{2.193 Re_{\theta c}} \qquad \textbf{(2.20)}$$

$$F_{onset2} = min\left(max\left(F_{onset1,} F_{onset1}^4\right), 2.0\right) \qquad \textbf{(2.21)}$$

$$F_{onset3} = max\left(1 - \left(\frac{R_T}{2.5}\right)^3, 0\right) \qquad \textbf{(2.22)}$$

$$F_{onset} = max(F_{onset2} - F_{onset3}, 0) \qquad \textbf{(2.23)}$$

$$F_{turb} = e^{-\left(\frac{R_T}{4}\right)^4} \qquad \textbf{(2.24)}$$

$Re_{\theta c}$ is the critical Reynolds number where the intermittency first starts to increase in the boundary layer. This occurs upstream of the transition Reynolds number $Re_{\theta t}$ and the difference between the two must be obtained from an empirical correlation. Both the F_{length} and $Re_{\theta c}$ correlations are function of $Re_{\theta t}$.

The constants for the intermittency equation are:

$$C_{a1} = 2; C_{e1} = 1; C_{a2} = 0.06; C_{e2} = 50; c_{\gamma 3} = 0.5; \sigma_{\gamma} = 1.0 \qquad \textbf{(2.25)}$$

The modification for separation-induced transition is:

$$\gamma_{sep} = min\left(C_{s1} max\left[\left(\frac{Re_V}{3.235 Re_{\theta c}}\right) - 1{,}0\right] F_{reattach}, 2\right) F_{\theta t} \qquad \textbf{(2.26)}$$

$$F_{reattach} = e^{-\left(\frac{R_T}{20}\right)^4} \qquad \textbf{(2.27)}$$

$$\gamma_{eff} = max(\gamma, \gamma_{sep}) \qquad \textbf{(2.28)}$$

Here, C_{s1} is a constant with a value 2.

The model constants in Eq. (2.28) have been adjusted from those of Menter Eq. in order to improve the predictions of separated flow transition. The main difference is that the constant that controls the relation between Re_V and $Re_{\theta c}$ was changed from 2.193, its value for a Blasius boundary layer to 3.235, the value at a separation point where the shape factor is 3.5. The boundary condition for γ at a wall is zero normal flux, while for an inlet, γ is equal to 1.0. The transport equation for the transition momentum thickness Reynolds number $Re_{\theta t}$ is

$$\frac{\partial(\rho Re_{\theta t})}{\partial t} + \frac{\partial(\rho U_j Re_{\theta t})}{\partial x_j} = P_{\theta t} + \frac{\partial}{\partial x_j}\left[\sigma_{\theta t}(\mu + \mu_t)\frac{\partial Re_{\theta t}}{\partial x_j}\right] \qquad \textbf{(2.29)}$$

The source term is defined as follows:

$$P_{\theta t} = c_{\theta t}\frac{\rho}{t}(Re_{\theta t} - Re_{\theta t})(1.0 - F_{\theta t}) \qquad \textbf{(2.30)}$$

$$t = \frac{500\mu}{\rho U^2} \qquad \textbf{(2.31)}$$

$$F_{\theta t} = min\left(max\left(F_{wake} e^{\left(-\frac{\gamma}{\delta}\right)^4}, 1.0 - \left(\frac{\gamma - 1/50}{1.0 - 1/50}\right)^2\right), 1.0\right) \qquad \textbf{(2.32)}$$

$$\theta_{BL} = \frac{Re_{\theta t}\mu}{\rho U} \qquad \textbf{(2.33)}$$

$$\delta_{BL} = \frac{15}{2}\theta_{BL} \tag{2.34}$$

$$\delta = \frac{50\Omega\gamma}{U}\delta_{BL} \tag{2.35}$$

$$Re_{\omega} = \frac{\rho\omega y^2}{\mu} \tag{2.36}$$

$$F_{wake} = e^{-\left(\frac{Re_{\omega}}{1E+5}\right)^2} \tag{2.37}$$

The model constants for $Re_{\theta t}$ equation are:

$$c_{\theta t} = 0.03\sigma_{\theta t} = 2.0 \tag{2.38}$$

The boundary condition for $Re_{\theta t}$ at a wall is zero flux, the boundary condition for $Re_{\theta t}$ at an inlet should be calculated from the empirical correlation based on the inlet turbulence intensity.

The model contains three empirical correlations. $Re_{\theta t}$ is the transition onset as observed in experiments. This has been modified from Menter Eq. in order to improve the predictions for natural transition. It is used in Eq. (2.29) F_{length} is the length of the transition zone and is substituted in Eq. (2.13). $Re_{\theta c}$ is the point where the model is activated in order to match both $Re_{\theta t}$ and F_{length}, and is used in Eq. (2.25).

$$Re_{\theta t} \quad = f(Tu, \lambda) \tag{2.39}$$

$$F_{length} = f(Re_{\theta t}) \tag{2.40}$$

$$Re_{\theta c} \quad = f(Re_{\theta t}) \tag{2.41}$$

The first empirical correlation is a function of the local turbulence intensity, and Thwaites' pressure gradient coefficient λ_{θ} is defined as

$$\lambda_{\theta} = (\theta^2/v)dU/ds \tag{2.42}$$

Where dU/ds is the acceleration in the streamwise direction.

The turbulence intensity specified at an inlet can decay quite rapidly depending on the inlet viscosity ratio (μ_t/μ) and hence turbulence eddy frequency. As a result, the local turbulence intensity downstream of the inlet can be much smaller than the inlet value. Typically, the larger the inlet viscosity ratio, the smaller the turbulent decay rate. However, if too large a viscosity ratio is specified (that is, > 100), the skin friction can deviate significantly from the laminar value. There is experimental evidence that suggests that this effect occurs physically; however, at this point it is not clear how accurately the transition model reproduces this behavior. For this reason, if possible, it is desirable to have a relatively low (that is, ≈ 1 – 10) inlet viscosity ratio and to estimate the inlet value of turbulence intensity such that at the leading edge of the blade/airfoil, the turbulence intensity has decayed to the desired value. The decay of turbulent kinetic energy can be calculated with the following analytical solution:

$$k = k_{inlet}(1 + \omega_{inlet}\beta t)^{\frac{-\beta^*}{\beta}} \tag{2.43}$$

For the SST turbulence model in the free stream the constants are:

$$\beta = 0.09 \text{ , } \beta^* = 0.0828 \tag{2.44}$$

The time scale can be determined as follows:

$$t = \frac{x}{V} \tag{2.45}$$

Where x is the streamwise distance downstream of the inlet and v is the mean convective velocity. The eddy viscosity is defined as:

$$\mu_t = \frac{\rho k}{\omega} \tag{2.46}$$

The decay of turbulent kinetic energy equation can be rewritten in terms of inlet turbulence intensity (Tu_{inlet}) and inlet eddy viscosity ratio (μ_t/μ) as follows:

$$Tu = \left(Tu_{inlet}^2 \left[1 + \frac{3\rho V x \beta Tu_{inlet}^2}{2\mu(\mu_t/\mu)_{inlet}}\right]^{-\frac{\beta^*}{\beta}} \right)^{0.5} \tag{2.47}$$

2.2 The Fluid-Structure Interaction

Fluid-Structure Interaction (FSI) is a general term that stands a phenomenon of exchange of kinetic energy between a moving fluid and a flexible structure. The extent of the energy exchange strongly depends on the flexibility and/or deformability of the structure and its resistance that is governed by geometric properties, elasticity and anchorage. In equal extent, the energy exchange depends also on the fluid, with its gradient and amplitude of the induced pressure waves, compressibility and other fluid state properties.

Fluid-Structure Interaction (FSI) analysis is an example of a multiphysic problem where the interaction between two different physics phenomena, done in separate analyses, is taken into account. From the perspective of the Mechanical application, an FSI analysis consists of performing a structural or thermal analysis in the application, with some of the loads (forces or temperatures, for example) coming from a corresponding fluid analysis or previous CFD analysis. In turn, the results of the mechanical analysis may be used as loads in a fluids analysis. The interaction between the two analyses typically takes place at the boundaries that the mechanical model shares with the fluids model. These boundaries of interaction are collectively called the fluid-structure interface. It is at this interface where the results of one analysis are passed to the other analysis as loads.

There are two different approaches for solving FSI problems using these softwares, the monolithic approach and the partitioned approach.

2.2.1 Monolithic approach

In this approach, both subproblems (fluid and structure) are formulated as one combined problem. The system of algebraic equations resulted from discretization of governing equation are solved. The interaction of fluid and structure at the interface is treated synchronously. This leads to the conservation of properties at the interface possible which increases the stability of the solution. Figure 2.2 represents the flow process of monolithic approach.

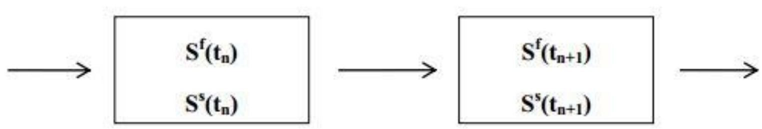

Figure 2.2 : Flow process of monolithic approach.

This approach is considered to be more robust than the partitioned approach. But this approach is computationally expensive and cannot take the advantage of software modularity as the partitioned method does.

2.2.2 Partitioned approach

The other choice for solving the FSI problems is the partitioned method. Here, both subproblems are solved separately which means the flow does not change while the structural solution is calculated. The equations governing the flow and the displacement of the structure are solved alternatingly in time with two distinct solvers. The intermediate fluid solution is prescribed as a boundary condition for the structure and vice versa, and the iteration continues until the convergence criterion is satisfied. At the interface (boundary between fluid and solid), the exchange of information occurs according to the type of coupling technique applied. Figure 2.3 explains the process of partitioned method.

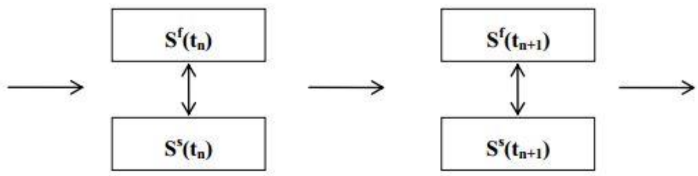

Figure 2.3 : Flow process of partitioned approach.

Due to the time lag between the integration of the fluid and structure domains, the interface conditions are implemented asynchronously which leads to a possibility of losing conservation of properties. But, this problem can be rectified by using mapping algorithms. Nevertheless, this allows the preservation of the software modularity.

As mentioned in the above paragraph, the information is exchanged at the interface between two solvers, this process is defined as the coupling, and this is of two types.

2.2.3 One-way coupling

The coupling is one-way if the motion of a fluid flow influences a solid structure but the reaction of a solid upon a fluid is negligible. The other way around is also possible. Figure 2.4 explains the one-way coupling method.

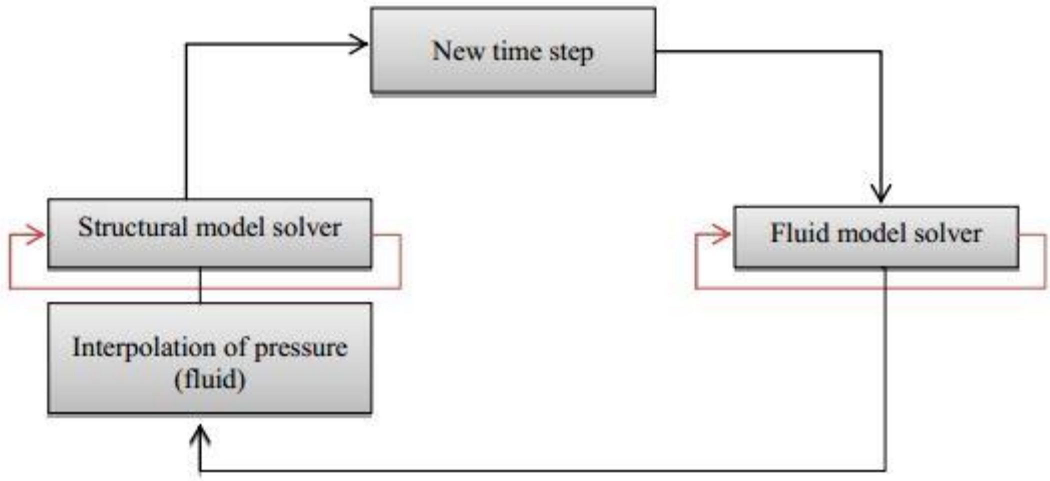

Figure 2.4 : One-way coupling method.

Initially, the fluid flow calculation is performed until convergence is reached. Then the resulting forces at the interface from fluid calculation are interpolated to the structural mesh. Next, the structural dynamic calculations are performed until the convergence criterion is met. This is repeated until the end time is reached.

2.2.4 Two-way coupling

This type of coupling is applied to the problem where the motion of a fluid influences a solid structure and at the same time the flow of fluid is influenced by reaction of a solid structure.

The work flow of the strong two-way coupling algorithm is shown in Figure 2.5. During the first time step, converged solutions of the fluid calculation provide the forces acting on the solid body. Then the forces are interpolated to the structural mesh like in one-way coupling and the solution from the structural solver is obtained with those fluid forces as boundary conditions. As a consequence the mesh is deformed according to the response of structure. These displacement values are interpolated to the fluid mesh which results in deformation of the fluid domain. This process is repeated until both force and displacement values are converged below the predetermined limit.

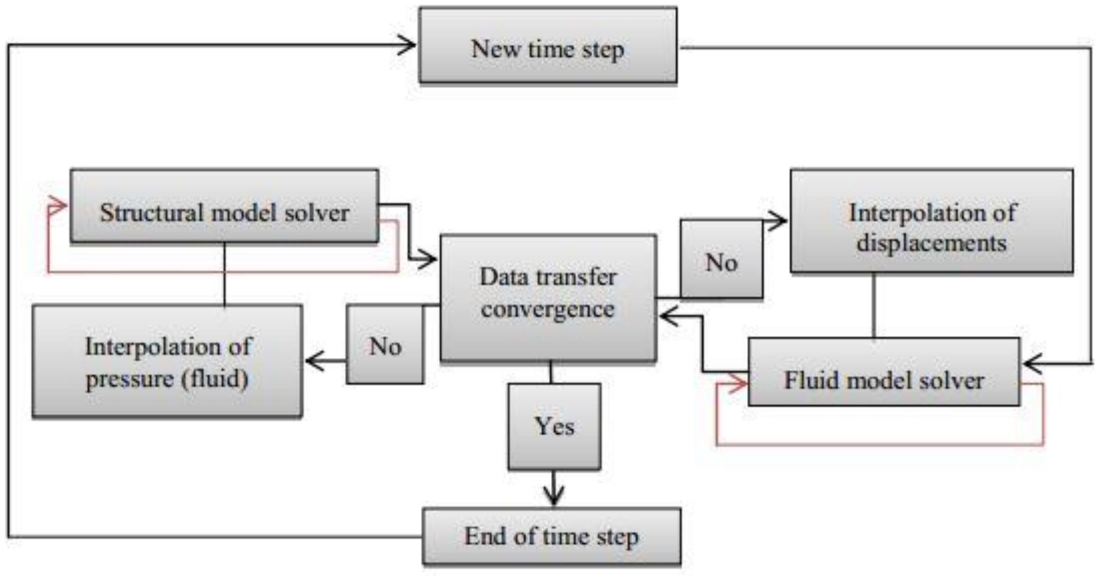

Figure 2.5 : Two-way coupling method.

2.3 Modal Analysis Theory

Modal analysis is a process to determine and identify the vibration characteristic of a mechanical system. Those characteristic are divided into three parameters which are frequency, mode shape and damping ratio. These characteristics can be defined as modal parameters or dynamic characteristic.

2.3.1 Single degree of freedom system

In order to understand modal analysis, single degree of freedom systems must be understood. In particular, the complete familiarity with single degree of freedom systems as presented and evaluated in the time, frequency (Fourier), and Laplace domains serves as the basis for many of the models that are used in modal parameter estimation. The single degree of freedom approach is obviously trivial for the modal analysis case. The importance of this approach results from the fact that the multiple degree of freedom case can be viewed as a linear superposition of single degrees of freedom systems. Single degree of freedom system is described in Figure 2.6.

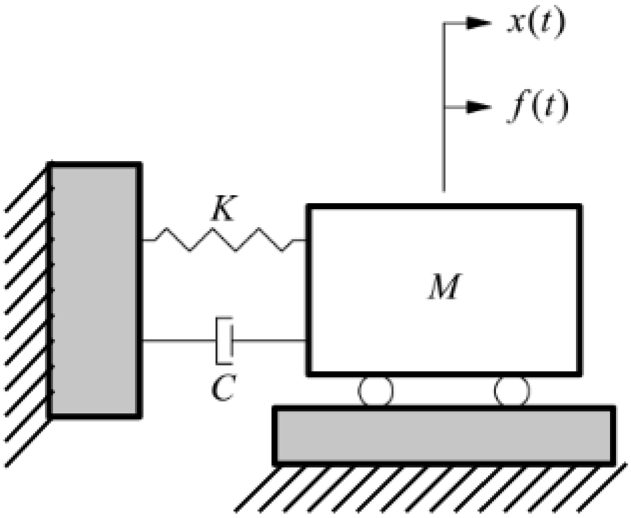

Figure 2.6 : Single degree of freedom system.

Free body diagram is shown in Figure 2.7.

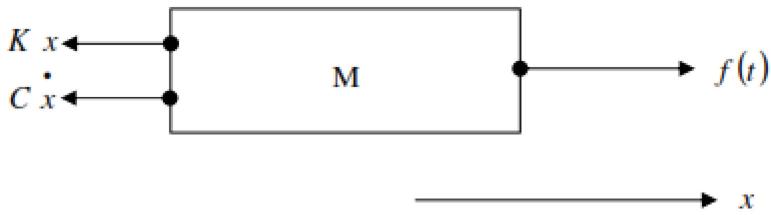

Figure 2.7 : Free body diagram.

The general mathematical representation of a single degree of freedom system is obtained from Newton's Law of Motion and expressed in Eq. (2.48), where total forces acting on the system is equaled to mass *M* times acceleration.

$$M\ddot{x}(t) + C\dot{x}(t) + Kx(t) = f(t) \quad \textbf{(2.48)}$$

Where;

- M = Mass of the system
- C = Damping of the system
- K = Stiffness of the system
- f(t) = General force function

By setting $f(t) = 0$, the homogeneous form of Eq. (2.49) can be solved.

$$M\ddot{x}(t) + C\dot{x}(t) + Kx(t) = 0 \quad \textbf{(2.49)}$$

From differential equation theory, the solution can be assumed to be of the form $x(t) = Xe^{st}$, where s is a complex valued number to be determined. Taking appropriate derivatives and substituting into Eq. (2.49) yields:

$$(Ms^2 + Cs + K)Xe^{st} = 0 \quad \textbf{(2.50)}$$

Thus, for a non-trivial solution:

$$Ms^2 + Cs + K = 0 \quad \textbf{(2.51)}$$

Where:

s = Complex-valued frequency variable (Laplace variable)

Eq. (2.51) is the characteristic equation of the system, whose roots λ_1 and λ_2 are:

$$\lambda_{1,2} = -\frac{C}{2M} \pm \left\{\left(\frac{C}{2M}\right)^2 - \left(\frac{K}{M}\right)\right\}^{\frac{1}{2}} \quad \textbf{(2.52)}$$

Thus the general solution of Eq. (2.49) is:

$$x(t) = Ae^{\lambda_1 t} + Be^{\lambda_2 t} \quad \textbf{(2.53)}$$

A and *B* are constants determined from the initial conditions imposed on the system at time *t=0*.

For most real structures, unless active damping systems are present, the damping ratio is rarely greater than ten percent. For this reason, all further discussion is restricted to underdamped systems ($\zeta<1$). With reference to Eq. (2.53), this means that the two roots, $\lambda_{1,2}$ are always complex conjugates. Also, the two coefficients (*A* and *B*) are complex conjugates of one another (*A* and A^*). For an underdamped system, the roots of the characteristic equation can be written as:

$$\lambda_1 = \sigma_1 + j\omega_1 \qquad \lambda_2 = \sigma_1 - j\omega_1 \quad \textbf{(2.54)}$$

Where;

- σ_1= Damping factor
- ω_1= Damped natural frequency

The roots of characteristic Eq. (2.51) can also be written as:

$$\lambda_1, \lambda_1^* = -\zeta_1 \Omega_1 \pm j\Omega_1 \sqrt{1-\zeta_1^2} \tag{2.55}$$

Where;

Ω_1 = Undamped natural frequency

ζ_1 = Percent damping with respect to critical damping

The damping factor, σ_1 , is defined as the real part of a root of the characteristic equation. This parameter has the same units as the imaginary part of the root of the characteristic equation, radians per second. The damping factor describes the exponential decay or growth of the oscillation. In real-world structures energy of the system is dissipated through damping mechanism. Therefore there is always exponential decay in oscillation. Exponential growth of the oscillation is theoretical and is not valid for real world structures.

Critical damping (c_c), is defined as being the damping which reduces the radical in the solution of the characteristic equation to zero. This form of damping representation is a physical approach and therefore involves the appropriate units for equivalent viscous damping.

$$\left(\frac{C_c}{2M}\right)^2 - \left(\frac{K}{M}\right) = 0 \ \rightarrow \ \frac{C_c}{2M} = \sqrt{\frac{K}{M}} \tag{2.56}$$

$$C_c = 2M\sqrt{\frac{K}{M}} = 2M\Omega_1 \tag{2.57}$$

The damping ratio, ζ , is the ratio of the actual system damping to the critical system damping. The damping ratio is dimensionless since the units are normalized.

$$\zeta_1 = \frac{C}{C_c} = \frac{-\sigma}{\Omega_1} \tag{2.58}$$

2.3.1.1 Time domain: impulse response function

The impulse response function of a single degree of freedom system can be determined from Eq. (2.53) assuming that the initial conditions are zero and that the system excitation, *f(t)*, is a unit impulse. The response of the system, *x(t)*, to such a unit impulse is known as the impulse response function, *h(t)*, of the system.

Therefore:

$$h(t) = Ae^{\lambda_1 t} + A^* e^{\lambda_1^* t} \qquad \textbf{(2.59)}$$

$$h(t) = e^{\sigma_1 t}\left[Ae^{(+jw_1 t)} + A^* e^{(-jw_1 t)}\right] \qquad \textbf{(2.60)}$$

Thus, the coefficients (A and A^*) control the amplitude of the impulse response, the real part of the pole is the decay rate and the imaginary part of the pole is the frequency of oscillation. Figure 2.8 illustrates the impulse response function, for a single degree of freedom system.

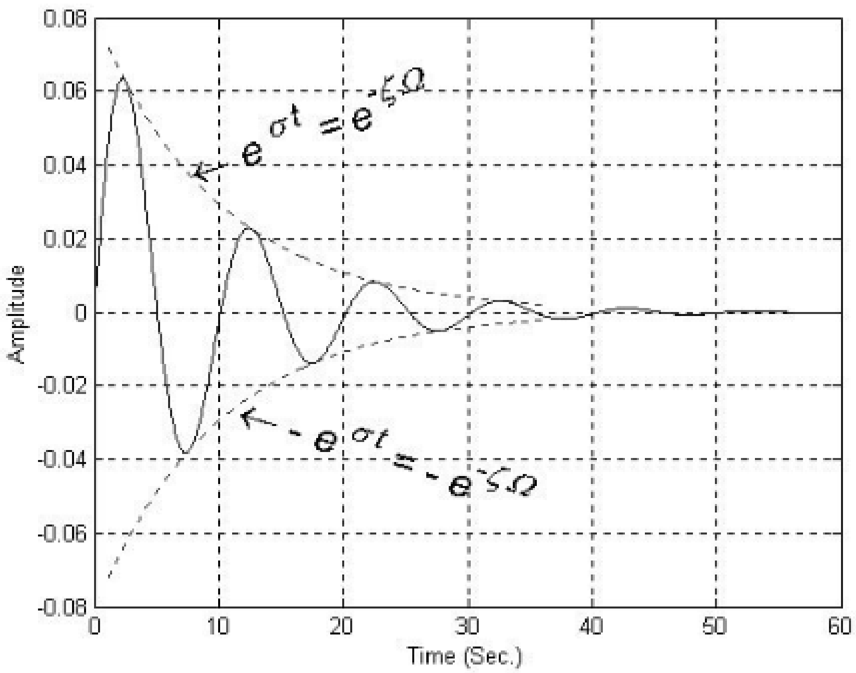

Figure 2.8 : Impulse response function.

2.3.1.2 Frequency domain: frequency response function

An equivalent equation of motion for Eq. (2.48) is determined for the Fourier or frequency (ω) domain. This representation has the advantage of converting a differential equation to an algebraic equation. This is accomplished by taking the Fourier transform (Meirovitch, 1996) of Eq. (2.48).

Letting the forcing function of Eq. (2.48) be in the form of

$$F(t) = F(\omega)e^{j\omega t} \tag{2.61}$$

Therefore the solution of Eq. (2.48) will be in the form of;

$$X(t) = X(\omega)e^{j\omega t} \tag{2.62}$$

Thus;

$$\dot{X}(t) = j\omega x(\omega)e^{j\omega t} \tag{2.63}$$

$$\ddot{X}(t) = -\omega^2 x(\omega)e^{j\omega t} \tag{2.64}$$

Substituting Eq. (2.62), Eq. (2.63) and Eq. (2.64) into Eq. (2.48) yields,

$$\left[-M\omega^2 x(\omega)e^{j\omega t} + jC\omega x(\omega)e^{j\omega t} + Kx(\omega)e^{j\omega t}\right] = F(\omega)e^{j\omega t} \tag{2.65}$$

After rearranging the common terms in Eq. (2.65);

$$[-M\omega^2 + jC\omega + K]X(\omega)e^{j\omega t} = F(\omega)e^{j\omega t} \tag{2.66}$$

Simplifying Equation (2.66) yields;

$$[-M\omega^2 + jC\omega + K]X(\omega) = F(\omega) \tag{2.67}$$

Restating Equation (2.67) yields:

$$B(\omega)X(\omega) = F(\omega) \tag{2.68}$$

Where,

$$B(\omega) = -M\omega^2 + jC\omega + K \tag{2.69}$$

Equation (2.68) states that the system response $X(\omega)$ is directly related to the system forcing function $F(\omega)$ though the quantity $B(\omega)$, the impedance function. If the system forcing function $F(\omega)$ and its response $X(\omega)$ are known, $B(\omega)$ can be calculated. That is:

$$B(\omega) = \frac{F(\omega)}{X(\omega)} \quad \textbf{(2.70)}$$

More frequently, the system response, $X(\omega)$ due to a known input $F(\omega)$ is of interest.

$$X(\omega) = \frac{F(\omega)}{B(\omega)} \quad \textbf{(2.71)}$$

Equation (2.71) becomes:

$$X(\omega) = H(\omega)F(\omega) \quad \textbf{(2.72)}$$

Where:

$$H(\omega) = \frac{1}{-M\omega^2 + jC\omega + K} \quad \textbf{(2.73)}$$

The quantity $H(\omega)$ is known as the "Frequency Response Function" of the system. The frequency response function relates Fourier transform of the system input to Fourier transform of the system response. From Equation (2.72), the frequency response function can be defined as:

$$H(\omega) = \frac{X(\omega)}{F(\omega)} \quad \textbf{(2.74)}$$

Going back to Equation (2.67), the frequency response function can be written as,

$$H(\omega) = \frac{1}{-M\omega^2 + jC\omega + K} = \frac{1/M}{-\omega^2 + j\left(\frac{C}{M}\right)\omega + \left(\frac{K}{M}\right)} \quad \textbf{(2.75)}$$

The denominator of Equation (2.75) is known as the "*characteristic equation*" of the system and is in the same form as Equation (2.51). The characteristic values of this complex equation are in general complex even though the equation is a function of a real valued independent variable "*ω*". The characteristic values of this equation are known as the complex roots of the characteristic equation or the complex poles of the system. These characteristic values are also called the "*modal frequencies*".

The frequency response function $H(\omega)$ can also be written as a function of the complex poles as follows:

$$H(\omega) = \frac{1/M}{(j\omega - \lambda_1)(j\omega - \lambda_1^*)} = \frac{A}{(j\omega - \lambda_1)} + \frac{A^*}{(j\omega - \lambda_1^*)} \quad \textbf{(2.76)}$$

Where;

λ_1 = Complex pole

$\lambda_1 = \sigma_1 + j\omega_1$

$\lambda_1^* = \sigma_1 - j\omega_1$

$\sigma_1 = -\zeta_1 \Omega_1$

$\omega_1 = \Omega_1 \sqrt{1 - \zeta_1^2}$

Since the frequency response function is a complex valued function of a real valued independent variable (ω), the frequency response function; real-imaginary, magnitude-phase graphs as shown in Figure 2.9 through Figure 2.12.

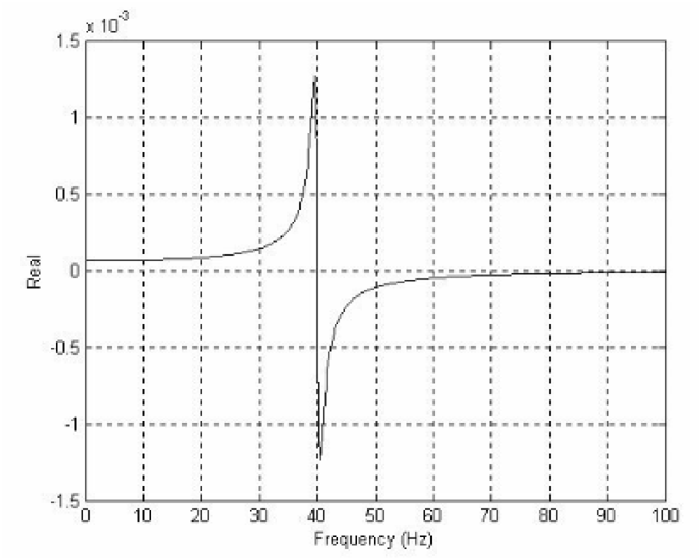

Figure 2.9 : Frequency response function (real).

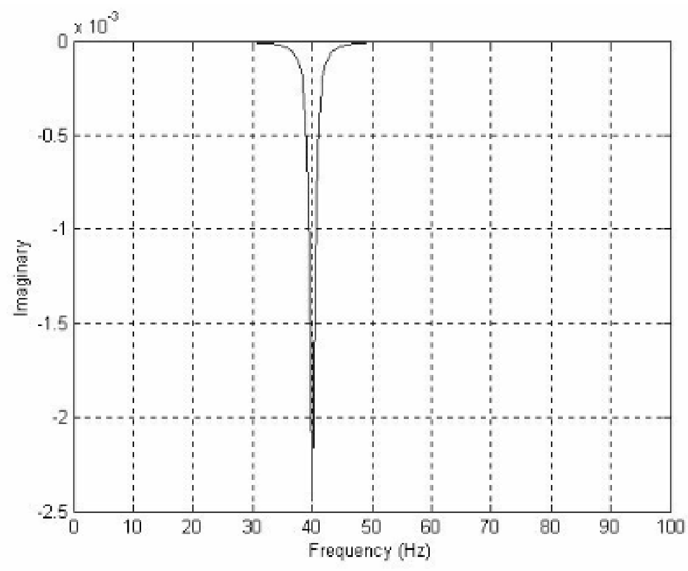

Figure 2.10 : Frequency response function (imaginary).

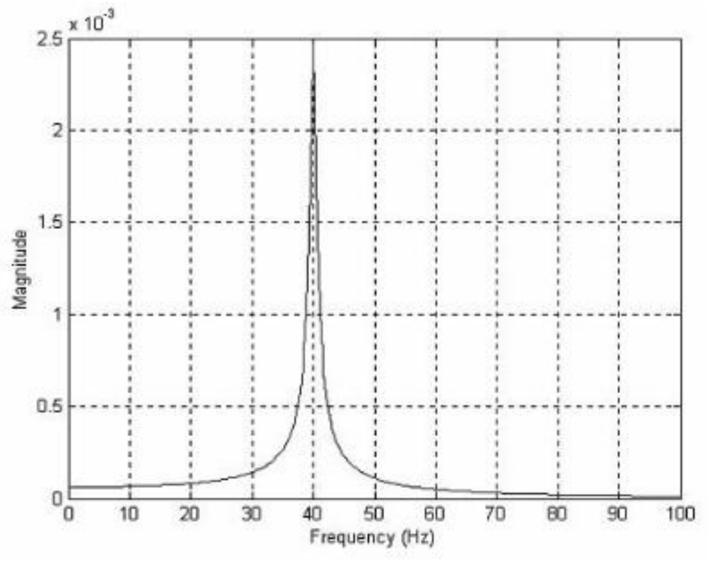

Figure 2.11 : Frequency response function (magnitude).

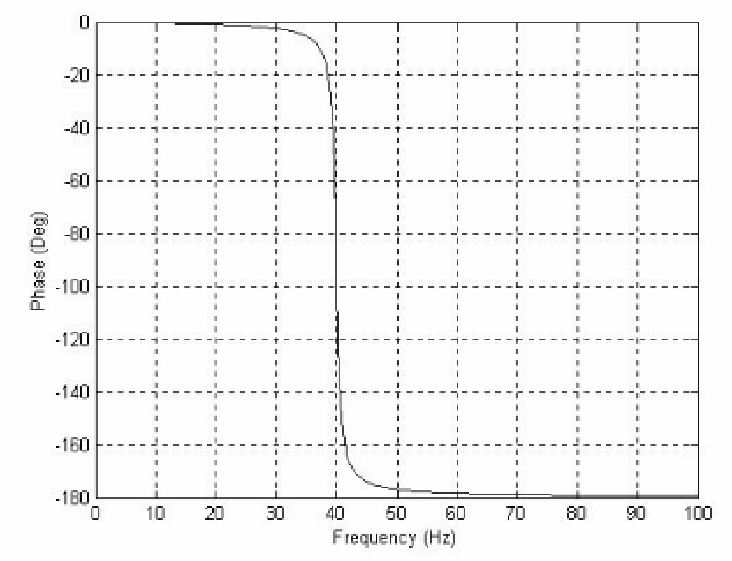

Figure 2.12 : Frequency response function (phase).

2.3.1.3 Laplace domain: transfer function

Just as in the previous case for the frequency domain, the equivalent information can be represented in Laplace domain by the way of Laplace transform. The only significant difference between the two domains are that Fourier transform is defined from negative infinity to positive infinity while Laplace transform is defined from zero to positive infinity with initial conditions. Laplace representation also has the advantage of converting a differential equation to an algebraic equation. Theory behind Laplace transform is shown in almost every classical text concerning vibrations (Meirovitch, 1996) The development using Laplace transform begins by taking Laplace transform of Equation (2.48). Thus Equation (2.48) becomes:

$$[Ms^2 + Cs + K]X(s) = F(s) + [Ms + C]X(0) + M\dot{X}(0) \qquad \textbf{(2.77)}$$

$X(0)$ and $\dot{X}(0)$ are the initial displacement and velocities at time $t = 0$, respectively. If the initial conditions are taken zero, Equation (2.77) becomes:

$$[Ms^2 + Cs + K]X(s) = F(s) \qquad \textbf{(2.78)}$$

Then, Equation (2.78) becomes:

$$B(s)X(s) = F(s) \qquad \textbf{(2.79)}$$

Where:

$$B(s) = Ms^2 + Cs + K \quad \textbf{(2.80)}$$

Therefore, using the same logic as in the frequency domain case, the transfer function can be defined in the same way that the frequency response function was defined previously.

$$X(s) = H(s)F(s) \quad \textbf{(2.81)}$$

Where:

$$H(s) = \frac{1}{Ms^2+Cs+K} \quad \textbf{(2.82)}$$

The quantity $H(s)$ is defined as the "*transfer function*" of the system. In other words, a transfer function relates Laplace transform of the system input to Laplace transform of the system response. From Equation (2.81), the transfer function can be defined as:

$$H(s) = \frac{X(s)}{F(s)} \quad \textbf{(2.83)}$$

Going back to Equation (2.71), the transfer function can be written:

$$H(s) = \frac{1}{Ms^2+Cs+K} = \frac{1/M}{s^2+\left(\frac{C}{M}\right)s+\left(\frac{K}{M}\right)} \quad \textbf{(2.84)}$$

Note that Equation (2.84) is valid under the assumption that the initial conditions are zero.

The denominator term is once again referred to as the characteristic equation of the system. As noted in the previous two cases, the roots of the characteristic equation are given in Equation (2.52). The transfer function, *H(s)*, can now be written, just as in the frequency response function case, as:

$$H(s) = \frac{1/M}{(s-\lambda_1)(s-\lambda_1^*)} = \frac{A}{(s-\lambda_1)} + \frac{A^*}{(s-\lambda_1^*)} \quad \textbf{(2.85)}$$

Since the transfer function is a complex valued function of complex independent variables, the transfer function is represented, as shown in Figures 2.13 through Figure 2.16, as a pair of surfaces. Remember that the variable (*s*) in Equation (2.77) is a complex variable, that is, it has a real part and imaginary part. Therefore, it can be viewed as a function of two variables which represent a surface.

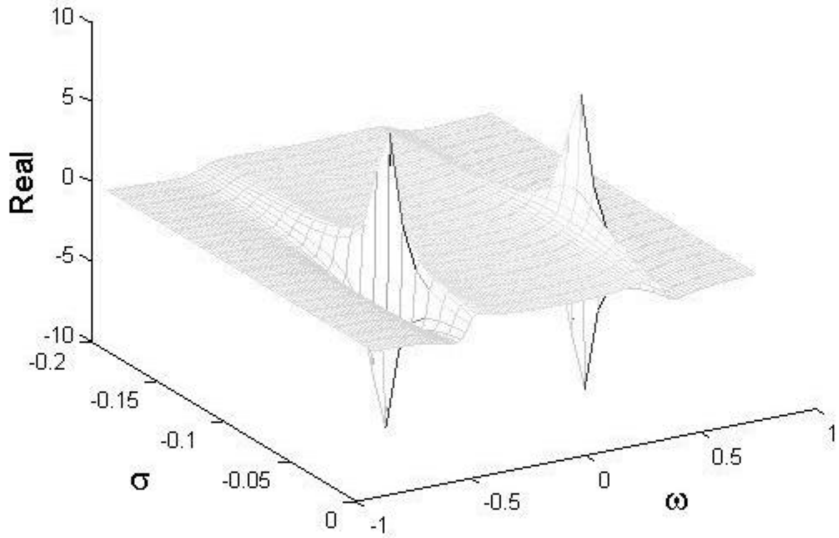

Figure 2.13 : Transfer function (real).

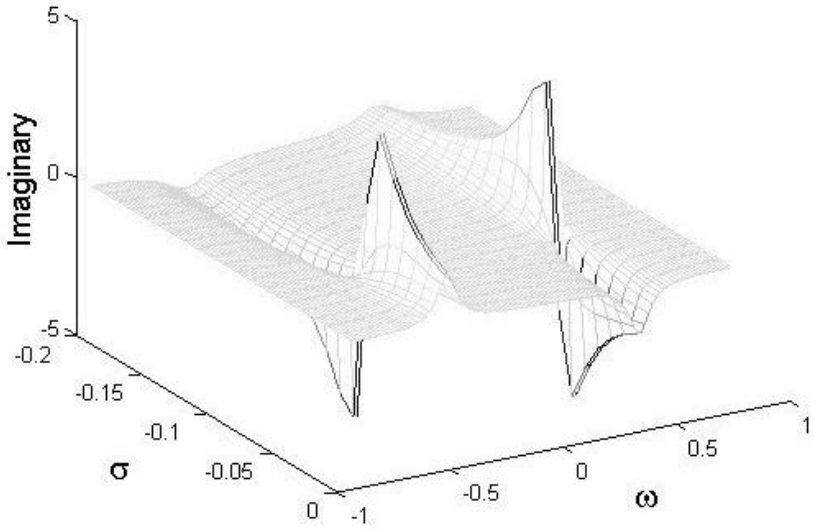

Figure 2.14 : Transfer function (imaginary).

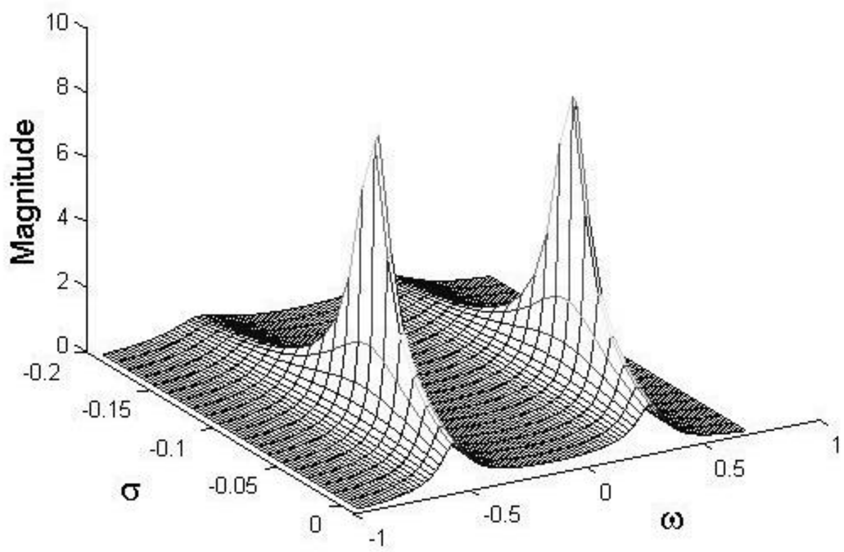

Figure 2.15 : Transfer function (magnitude).

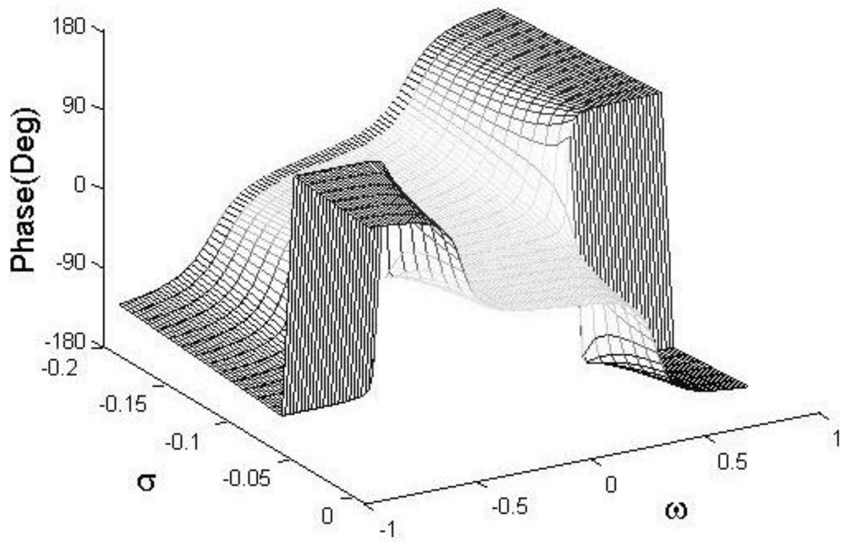

Figure 2.16 : Transfer function (phase).

The definition of undamped natural frequency, damped natural frequency, damping factor, percent of critical damping, and residue are all relative to the information represented by Figure 2.13 through Figure 2.16. The projection of this information onto the plane of zero amplitude yields the information as shown in Figure 2.17.

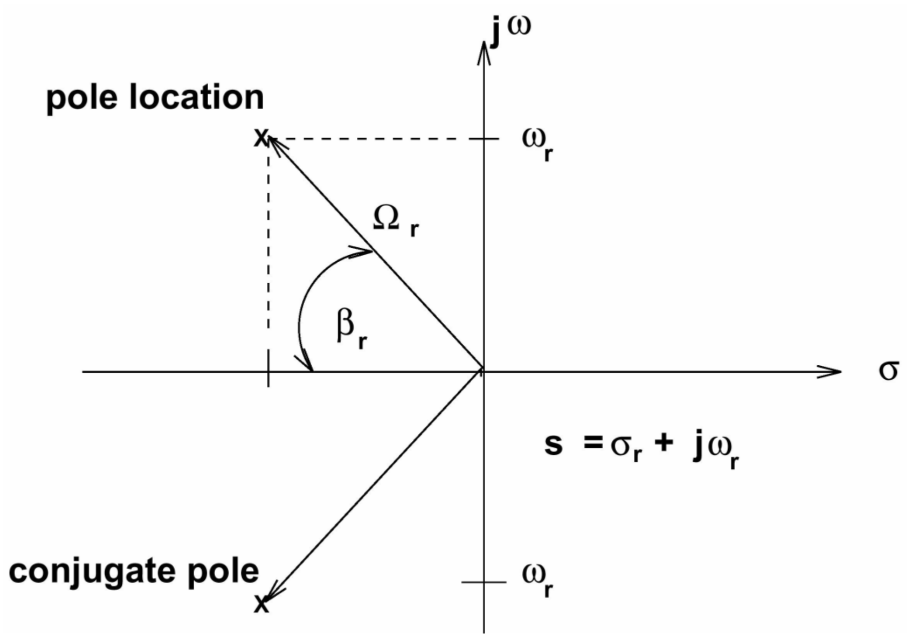

Figure 2.17 : Transfer function (laplace plane projection).

Where;

$\sigma_r =$ Damping ratio

$\omega_r =$ Damped natural frequency

$\Omega_r =$ Undamped natural frequency

$\zeta_r = cos\beta_b =$ Damping factor (percent of critical damping)

The concept of residues is now defined in terms of the partial fraction expansion of the transfer function equation. Equation (2.85) can be expressed in terms of partial fractions as follows:

$$H(s) = \frac{1/M}{(s-\lambda_1)(s-\lambda_1^*)} = \frac{A}{(s-\lambda_1)} + \frac{A^*}{(s-\lambda_1^*)} \qquad \textbf{(2.86)}$$

The residues of the transfer function are defined as being the constants A and A^*. The terminology and development of residues comes from the evaluation of analytic functions in complex analysis. The residues of the transfer function are directly related to the amplitude of the impulse response function. In general, the residue A can be a complex quantity.

It can be noted that Laplace transform formulation is simply the general case of Fourier transform development if the initial conditions are zero. The frequency response function is the part of the transfer function evaluated along the $s = j\omega$ axis.

From an experimental point of view, the transfer function is not estimated from measured input-output data (experimental modal analysis). Instead, the frequency response function is actually estimated via the discrete Fourier transform.

2.3.2 Multiple degree of freedom systems

The real applications of modal analysis concepts begin when a continuous, non-homogeneous structure is described as a lumped mass, multiple degree-of-freedom systems. At this point, the modal frequencies, the modal damping, and the modal vectors, or relative patterns of motion, can be found via an estimate of the mass, damping, and stiffness matrices or via the measurement of the associated frequency response functions. The two-degree of freedom system, shown in Figure 2.18, is the most basic example of a multiple degree of freedom system. This example is useful for discussing modal analysis concepts since a theoretical solution can be formulated in terms of the mass, stiffness and damping matrices or in terms of the frequency response functions.

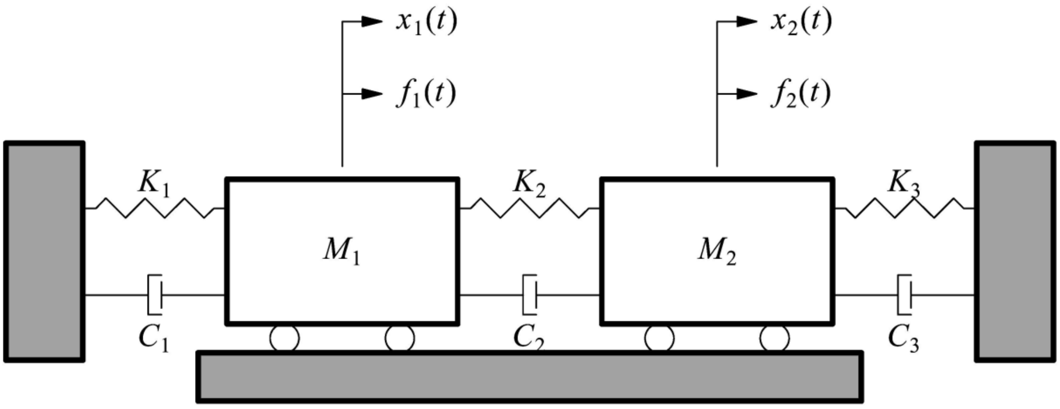

Figure 2.18 : Multiple degree of freedom system.

The equations of motion for the system in Figure 2.18, using the matrix notation, are as follows:

$$\begin{bmatrix} M_1 & 0 \\ 0 & M_2 \end{bmatrix}\begin{bmatrix} \ddot{x}_1 \\ \ddot{x}_2 \end{bmatrix} + \begin{bmatrix} (C_1 + C_2) & -C_2 \\ -C_2 & (C_2 + C_3) \end{bmatrix}\begin{bmatrix} \dot{x}_1 \\ \dot{x}_2 \end{bmatrix} + \begin{bmatrix} (K_1 + K_2) & -K_2 \\ -K_2 & (K_2 + K_3) \end{bmatrix}\begin{bmatrix} x_1 \\ x_2 \end{bmatrix}$$

$$= \begin{bmatrix} f_1 \\ f_2 \end{bmatrix} \quad \textbf{(2.87)}$$

The process of solving Equation (2.87) when the mass, damping, and stiffness matrices are known is shown in almost every classical text concerning vibrations.

The development of the frequency response function solution for the multiple degree of freedom case is similar to the single degree-of-freedom case, which relates the mass, damping, and stiffness matrices to a transfer function model involving multiple degrees of freedom. Just as in the analytical case, where the ultimate solution can be described in terms of one degree of freedom systems, the frequency response functions between any input and response degree of freedom can be represented as a linear superposition of the single degree of freedom models derived previously.

As a result of the linear superposition concept, the equations for the impulse response function, the frequency response function, and the transfer function for the multiple degree of freedom system are defined as follows:

Impulse response function (Time domain):

$$[h(t)] = \sum_{r=1}^{N} [A_r] e^{\lambda_r t} + [A_r^*] e^{\lambda_r^* t} = \sum_{r=1}^{2N} [A_r] e^{\lambda_r t} \quad \textbf{(2.88)}$$

Frequency response function (Frequency domain):

$$[H(\omega)] = \sum_{r=1}^{N} \frac{[A_r]}{j\omega - \lambda_r} + \frac{A_r^*}{j\omega - \lambda_r} = \sum_{r=1}^{2N} \frac{[A_r]}{j\omega - \lambda_r} \quad \textbf{(2.89)}$$

Transfer function (Laplace domain):

$$[H(s)] = \sum_{r=1}^{N} \frac{[A_r]}{s - \lambda_r} + \frac{A_r^*}{s - \lambda_r} = \sum_{r=1}^{2N} \frac{[A_r]}{s - \lambda_r} \quad \textbf{(2.90)}$$

Where:

$t =$ Time variable

$\omega =$ Frequency variable

$s =$ Laplace variable

$p =$Measured degree of freedom (output)

$q =$ Measured degree of freedom (input)

$r =$ Modal vector number

$A_{pqr} =$ Residue

$A_{pqr} = Q_r \Psi_{pr} \Psi_{qr}$

Q_r = Modal scaling factor

Ψ_{pr} = Modal coefficient

λ_r = System pole

N = Number of positive modal frequencies

It is important to note that the residue, A_{pqr} , in Equation (2.88) through Equation (2.90) is the product of the modal deformations at the input q and response p degrees of freedom and a modal scaling factor for mode r. Therefore, the product of these three terms is unique but each of the three terms by themselves is not unique. This is consistent with the arbitrary normalization of the modal vectors. Modal scaling, Q_r, refers to the relationship between the normalized modal vectors and the absolute scaling of the mass matrix (analytical case) and/or the absolute scaling of the residue information (experimental case). Modal scaling is normally presented as modal mass or *modal A*.

The driving point residue, A_{pqr}, is particularly important in deriving the modal scaling.

$$A_{pqr} = Q_r \Psi_{pr} \Psi_{qr} = Q_r \Psi_{qr}^2 \tag{2.91}$$

For undamped and proportionally damped systems, the r-th modal mass of a multi degree of freedom system can be defined as:

$$M_r = \frac{1}{j2Q_r\omega_r} = \frac{\Psi_{pr}\Psi_{qr}}{j2A_{pqr}\omega_r} \tag{2.92}$$

Where:

M_r = Modal mass

Q_r = Modal scaling constant

ω_r = Damped natural frequency

If the largest scaled modal coefficient is equal to unity, Equation (2.92) will also compute a quantity of modal mass that has physical significance. The physical significance is that the quantity of modal mass computed under these conditions will be a number between zero and the total mass of the system. Therefore, under this scaling condition, the modal mass can be viewed as the amount of mass that is participating in each mode of vibration. Obviously, for a translational rigid body mode of vibration, the modal mass should be equal to the total mass of the system.

The modal mass defined in Equation (2.92) is developed in terms of displacement over force units. If measurements, and therefore residues, are developed in terms of any other units (*velocity over force or acceleration over force*), Equation (2.92) will have to be altered accordingly.

Once the modal mass is known, the modal damping and modal stiffness can be obtained through the following single degree of freedom equations:

Modal damping

$$C_r = 2\sigma_r M_r \qquad \textbf{(2.93)}$$

Modal stiffness

$$K_r = (\sigma_r^2 + \omega_r^2)M_r = \Omega_r^2 M_r \qquad \textbf{(2.94)}$$

For systems with non-proportional damping, modal mass cannot be used for modal scaling. For non-proportional case, and increasingly for undamped and proportionally damped cases as well, the *modal A* scaling factor is used as the basis for the relationship between the scaled modal vectors and the residues determined from the measured frequency response functions. This relationship is as follows:

Modal A

$$M_{A_r} = \frac{\Psi_{pr}\Psi_{qr}}{A_{pqr}} = \frac{1}{Q_r} \qquad \textbf{(2.95)}$$

This definition of *modal A* is also developed in terms of displacement over force units. Once *modal A* is known, *modal B* can be obtained through the following single degree of freedom equation:

Modal B

$$M_{B_r} = -\lambda_r M_{A_r} \qquad \textbf{(2.96)}$$

For undamped and proportionally damped systems, the relationship between modal mass and *modal A* scaling factors can be stated.

$$M_{A_r} = \pm 2 M_r \omega_r \tag{2.97}$$

In general, modal vectors are considered to be dimensionless since they represent relative patterns of motion. Therefore, the modal mass or modal A scaling terms carry the units of the respective measurement. For example, the development of the frequency response is based upon displacement over force units. The residue must therefore, have units of length over force-seconds. Since the modal A scaling coefficient is inversely related to the residue, modal A will have units of force-seconds over length. This unit combination is the same as mass over seconds. Likewise, since modal mass is related to modal A, for proportionally damped systems, through a direct relationship involving the damped natural frequency, the units on modal mass are mass units as expected.

2.4 Acoustic-Structure Analysis

This chapter investigates the analysis of acoustic-structure systems, here limited to systems consisting of a flexible structure in contact with an enclosed acoustic cavity, within the finite element environment. In the sections following, the governing equations of the acoustic-structure problem are given and the finite element formulation of this problem is derived.

2.4.1 Governing equations

For the acoustic-structure system, the structure is described by the differential equation of motion for a continuum body assuming small deformations and the fluid by the acoustic wave equation. Coupling conditions at the boundary between the structural and fluid domains ensure the continuity in displacement and pressure between the domains. The governing equations and boundary conditions can, as for example, was described in detail by (Carlsson, 1992) be written:

$$\text{Structure:} \quad \begin{cases} \tilde{\nabla}^T \sigma_S + b_S = \rho_S \dfrac{\partial^2 u_S}{\partial t^2} & \Omega_S \\ + \, Boundary \; and \; initial \; conditions \end{cases}$$

$$\text{Fluid:} \quad \begin{cases} \dfrac{\partial^2 p_F}{\partial^2 t} - c_0^2 \nabla^2 p_F = c_0^2 \dfrac{\partial q_F}{\partial t} & \Omega_F \\ + \, Boundary \; and \; initial \; conditions \end{cases}$$

Coupling: $\begin{cases} u_S = u_F & \partial\Omega_{FS} \\ \sigma_S = -p_F & \partial\Omega_{FS} \end{cases}$

The variables and materials parameters are defined in the following sections, where also the finite element formulation of this coupled problem derived.

The finite element formulation of both the continuum body and the acoustic fluid are used for the modelling of fan louver and freezer cavity. The structure of interest in most acoustic-structure problems is two dimensional and is therefore often described by plate or shell theory.

2.4.2 Finite element formulation

2.4.2.1 Structural domain

The structure is described by the equation of motion for continuum body. The finite element formulation is derived with the assumption of small displacement. This presentation follows the matrix notation used by (Ottosen and Petersson, 1992).

For a continuum material the equation of motion can be written

$$\tilde{\nabla}^T \sigma_S + b_S = q_S \tag{2.98}$$

With the displacement, u_S , the body force, b_S , and the inertia force, q_S ,

$$u_S = \begin{bmatrix} u_1^S \\ u_2^S \\ u_3^S \end{bmatrix} ; b_S = \begin{bmatrix} b_1^S \\ b_2^S \\ b_3^S \end{bmatrix} ; q_S = \rho_S \frac{\partial^2 u_S}{\partial t^2} \tag{2.99}$$

Where p_S is the density of the material. The differential operator $\tilde{\nabla}$ can be written

$$\tilde{\nabla} = \begin{bmatrix} \frac{\partial}{\partial x_1} & 0 & 0 \\ 0 & \frac{\partial}{\partial x_2} & 0 \\ 0 & 0 & \frac{\partial}{\partial x_3} \\ \frac{\partial}{\partial x_2} & \frac{\partial}{\partial x_1} & 0 \\ \frac{\partial}{\partial x_3} & 0 & \frac{\partial}{\partial x_1} \\ 0 & \frac{\partial}{\partial x_3} & \frac{\partial}{\partial x_2} \end{bmatrix} \tag{2.100}$$

The Green-Lagrange strain tensor, E_S , and the Cauchy stress tensor S_S are defined as

$$E_S = \begin{bmatrix} \varepsilon_{11}^S & \epsilon_{12}^S & \varepsilon_{13}^S \\ \epsilon_{12}^S & \varepsilon_{22}^S & \varepsilon_{23}^S \\ \varepsilon_{13}^S & \varepsilon_{23}^S & \varepsilon_{33}^S \end{bmatrix} ; \; S_S = \begin{bmatrix} \sigma_{11}^S & \sigma_{12}^S & \sigma_{13}^S \\ \sigma_{12}^S & \sigma_{22}^S & \sigma_{23}^S \\ \sigma_{13}^S & \sigma_{23}^S & \sigma_{33}^S \end{bmatrix} \quad \textbf{(2.101)}$$

And in matrix notations the strains and stresses can be written

$$\varepsilon_S = \begin{bmatrix} \varepsilon_{11}^S \\ \varepsilon_{22}^S \\ \varepsilon_{33}^S \\ \gamma_{12}^S \\ \gamma_{13}^S \\ \gamma_{23}^S \end{bmatrix} ; \quad \sigma_S = \begin{bmatrix} \sigma_{11}^S \\ \sigma_{22}^S \\ \sigma_{33}^S \\ \sigma_{12}^S \\ \sigma_{13}^S \\ \sigma_{23}^S \end{bmatrix} \quad \textbf{(2.102)}$$

Where $\gamma_{12}^S = 2\varepsilon_{12}^S$, $\gamma_{13}^S = 2\varepsilon_{13}^S$ and $\gamma_{23}^S = 2\varepsilon_{23}^S$. The kinematic relations, the relations between the displacements and strains, can be written

$$\varepsilon_S = \tilde{\nabla} u_S \quad \textbf{(2.103)}$$

For an isotropic material, the stresses and strains are related by the constitutive matrix D_S given by

$$\sigma_S = D_S \varepsilon_S \quad \textbf{(2.104)}$$

Where

$$D_S = \begin{bmatrix} \lambda + 2\mu & \lambda & \lambda & 0 & 0 & 0 \\ \lambda & \lambda + 2\mu & \lambda & 0 & 0 & 0 \\ \lambda & \lambda & \lambda + 2\mu & 0 & 0 & 0 \\ 0 & 0 & 0 & \mu & 0 & 0 \\ 0 & 0 & 0 & 0 & \mu & 0 \\ 0 & 0 & 0 & 0 & 0 & \mu \end{bmatrix} \quad \textbf{(2.105)}$$

The Lame coefficients, λ and μ, are expressed in the modulus of elasticity, E, the shear modulus, G, and Poisson's ratio, ν by

$$\lambda = \frac{\nu E}{(1+\nu)(1-2\nu)} \quad \textbf{(2.106)}$$

$$\mu = G = \frac{E}{2(1+\nu)} \quad \textbf{(2.107)}$$

To arrive at the finite element formulation for the structural domain, the weak form of the differential equation is derived. This can be done by multiplying Eq. (2.98) with a weight function, $\nu_S = [\nu_1 \quad \nu_2 \quad \nu_3]^T$, and integrating over the material domain, Ω_S,

$$\int_{\Omega_S} \nu_S^T \left(\breve{\nabla}^T \sigma_S - \rho_S \frac{\partial^2 u_S}{\partial t^2} + b_S \right) dV = 0 \qquad \textbf{(2.108)}$$

Using Green-Gauss theorem on the first term in Eq. (2.108) gives

$$\int_{\Omega_S} \nu_S^T \breve{\nabla}^T \sigma_S dV = \int_{\partial\Omega_S} (\nu_S)^T t_S dS - \int_{\Omega_S} (\breve{\nabla} \nu_S)^T \sigma_S dV \qquad \textbf{(2.109)}$$

The surface traction vector t_S related to the Cauchy stress tensor, S_S , by

$$t_S = S_S n_S \qquad \textbf{(2.110)}$$

Where n_S is the boundary normal vector pointing outward from the structural domain. The weak form of the problem can be written

$$\int_{\Omega_S} \nu_S^T \rho_S \frac{\partial^2 u_S}{\partial t^2} dV + \int_{\Omega_S} (\breve{\nabla} \nu_S)^T \sigma_S dV - \int_{\partial\Omega_S} (\nu_S)^T t_S dS - \int_{\Omega_S} \nu_S^T b_S dV = 0 \quad \textbf{(2.111)}$$

Introducing the finite element approximation of the displacement d_S and weight functions c_S by

$$u_S = N_S d_S \quad ; \quad \nu_V = N_S c_S \qquad \textbf{(2.112)}$$

Where N_S contains the finite element shape functions for the structural domain, the strains can be expressed as

$$\varepsilon_S = \breve{\nabla} N_S d_S \qquad \textbf{(2.113)}$$

This gives the finite element formulation for the structural domain, when described as a continuum body

$$\int_{\Omega_S} N_S^T \rho_S N_S dV \ddot{d}_S + \int_{\Omega_S} (\breve{\nabla} N_S)^T D_S \breve{\nabla} N_S dV d_S = \int_{\partial\Omega_S} N_S^T t_S dS + \int_{\Omega_S} N_S^T b_S dV \quad \textbf{(2.114)}$$

And the governing system of equations can be written

$$M_S \ddot{d}_S + K_S d_S = f_F + f_b \qquad \textbf{(2.115)}$$

Where

$$M_S = \int_{\Omega_S} N_S^T \rho_S N_S dV \quad ; \quad K_S = \int_{\Omega_S} (\breve{\nabla} N_S)^T D_S \breve{\nabla} N_S dV \qquad \textbf{(2.116)}$$

$$f_F = \int_{\partial\Omega_S} N_S^T t_S dS \quad ; \quad f_b = \int_{\Omega_S} N_S^T b_S dV \qquad \textbf{(2.117)}$$

2.4.2.2 Acoustic domain

In acoustic fluid-structure interaction problems, the structural dynamic equation must be considered along with the Navier-Stokes equations of fluid momentum and the flow continuity equation. The governing equations for an acoustic fluid are derived using the following assumptions for the compressible fluid.

- The fluid is inviscid.
- The fluid only undergoes small translations.
- The fluid is irrotational.

Thereby, the governing equations for an acoustic fluid are, the equation of motion,

$$\rho_0 \frac{\partial^2 u_F(t)}{\partial t^2} + \nabla P_F(t) = 0 \qquad \textbf{(2.118)}$$

The continuity equation,

$$\frac{\partial \rho_F(t)}{\partial t} + \rho_0 \nabla \frac{\partial u_F(t)}{\partial t} = q_F(t) \qquad \textbf{(2.119)}$$

And the constitutive equation,

$$P_F(t) = c_0^2 \rho_F(t) \qquad \textbf{(2.120)}$$

Here $u_F(t)$ is the displacement, $P_F(t)$ is the dynamic pressure, $\rho_F(t)$ is the dynamic density and $q_F(t)$ is the added fluid mass per unit volume. ρ_0 is the static density and c_0 is the speed of sound. ∇ denotes a gradient of a variable, i.e.,

$$\nabla = \begin{bmatrix} \frac{\partial y}{\partial x_1} & \frac{\partial y}{\partial x_2} & \frac{\partial y}{\partial x_3} \end{bmatrix}^T \qquad \textbf{(2.121)}$$

The nonhomogeneous wave equation can be derived from equations (2.118) – (2.120). Differentiating equation (2.119) with respect to time and using (2.120) gives

$$\frac{1}{c_o^2}\frac{\partial^2 P_F}{\partial t^2} + \rho_0 \nabla \left(\rho_0 \frac{\partial^2 u_F}{\partial t^2}\right) = \frac{\partial q_F}{\partial t} \quad \textbf{(2.122)}$$

Substituting (2.118) into this expression gives the nonhomogeneous wave equation expressed in acoustic pressure p_F.

$$\frac{\partial^2 \mathrm{P_F}}{\partial \mathrm{t}^2} - \mathrm{c_o^2}\nabla^2 p_\mathrm{F} = \mathrm{c_0^2}\frac{\partial \mathrm{q_F}}{\partial \mathrm{t}} \quad \textbf{(2.123)}$$

Where $\nabla^2 = \partial^2/\partial x_1^2 + \partial^2/\partial x_2^2 + \partial^2/\partial x_3^2$.

The finite element formulation of equation (2.123) is derived by multiplying with a test function, u_F , and integrating over a volume Ω_F .

$$\int_{\Omega_F} u_F \left(\frac{\partial^2 P_F}{\partial t^2} - c_o^2 \nabla^2 p_\mathrm{F} - \mathrm{c_0^2}\frac{\partial \mathrm{q_F}}{\partial \mathrm{t}}\right) dV = 0 \quad \textbf{(2.124)}$$

And with Green’s theorem the weak formulation is achieved.

$$\int_{\Omega_F} u_F \frac{\partial^2 P_F}{\partial^2 t} dV + c_o^2 \int_{\Omega_F} \nabla u_F \nabla p_F dV = c_o^2 \int_{\partial\Omega_F} u_F \nabla p_F n_F dA + c_o^2 \int_{\Omega_F} u_F \frac{\partial q_F}{\partial t} dV \quad \textbf{(2.125)}$$

Where the boundary normal vector n_F points outward from the fluid domain. The finite element method approximates the pressure field and the weight function by

$$p_F = N_F p_F \quad ; \quad u_F = N_F c_F \quad \textbf{(2.126)}$$

Where p_F contains the modal pressures, c_F the nodal weights and N_F contains the finite element shape functions for the fluid domain. Inserting this into equation (2.125) and noting that c_F is arbitrary gives

$$\int_{\Omega_F} N_F^T N_F dV \ddot{p}_F + c_0^2 \int_{\Omega_F} (\nabla N_F)^T \nabla N_F dV p_F = c_0^2 \int_{\partial\Omega_F} N_F^T \nabla p_F n_F dS +$$

$$c_0^2 \int_{\Omega_F} N_F^T \frac{\partial q_F}{\partial t} dV \quad \textbf{(2.127)}$$

The system of equations for an acoustic domain becomes

$$M_F \ddot{P} + K_F P = f_q + f_s \quad \textbf{(2.128)}$$

Where

$$M_F = \int_{\Omega_F} N_F^T N_F dV \quad ; \quad K_F = c_0^2 \int_{\Omega_F} (\nabla N_F)^T \nabla N_F dV \quad \textbf{(2.129)}$$

$$f_S = c_0^2 \int_{\partial\Omega_F} N_F^T n_F^T \nabla p dS \quad ; \quad f_q = c_0^2 \int_{\Omega_F} N_F^T \frac{\partial q}{\partial t} dV \qquad \textbf{(2.130)}$$

2.4.2.3 The coupled acoustic-structure system

At the boundary between the structural and fluid domains, denoted Ω_{SF} , the fluid particles and the structure moves together in the normal direction of the boundary. Introducing the normal vector $n_F = -n_S$, the displacement boundary condition can be written

$$u_S n = u_F n \qquad \textbf{(2.131)}$$

And the continuity in pressure

$$\sigma_S = -p_F \qquad \textbf{(2.132)}$$

Where p_F is the acoustic fluid pressure. The structural stress tensor at the boundary $\partial\Omega_{SF}$ thus becomes

$$S_S = -p_F \begin{bmatrix} 1 & 0 & 0 \\ 0 & 1 & 0 \\ 0 & 0 & 1 \end{bmatrix} \qquad \textbf{(2.133)}$$

And the structural force term providing the coupling to the fluid domain, f_F , (in equation (2.115)), can be written

$$f_F = \int_{\partial\Omega_{SF}} N_S^T (-p_F) \begin{bmatrix} 1 & 0 & 0 \\ 0 & 1 & 0 \\ 0 & 0 & 1 \end{bmatrix} n_S dS = \int_{\partial\Omega_{SF}} N_S^T n p_F dS = \int_{\partial\Omega_{SF}} N_S^T n N_F p_F dS$$

(2.134)

Note that the structural boundary normal vector n_S is replaced with the normal vector n pointing in the opposite direction. The force acting on the structure is expressed in the acoustic fluid pressure.

For the fluid partition the coupling is introduced in the force term f_S (in equation (2.128)). Using the relation between pressure and acceleration in the fluid domain

$$\nabla p_F = -\rho_0 \frac{\partial^2 u_F t}{\partial t^2} \qquad \textbf{(2.135)}$$

And the boundary condition in equation (2.131), the force acting on the fluid can be described in terms of structural acceleration

$$n^T \nabla p_F = -\rho_0 n^T \frac{\partial^2 u_F}{\partial t^2} = -\rho_0 n^T \frac{\partial^2 u_S}{\partial t^2} = -\rho_0 n^T N_S \ddot{d}_S \qquad \textbf{(2.136)}$$

And the boundary force term of the acoustic fluid domain, f_S , can be expressed in structural acceleration

$$f_S = -c_0^2 \int_{\partial\Omega_{FS}} N_F^T n^T \nabla p_F dS = -\rho_0 c_o^2 \int_{\partial\Omega_{FS}} N_F^T n^T N_S dS \ddot{d}_S \qquad \textbf{(2.137)}$$

The introduction of a spatial coupling matrix

$$H_{SF} = \int_{\partial\Omega_{SF}} N_S^T n N_F dS \qquad \textbf{(2.138)}$$

Allows the coupling forces to be written as

$$f_F = H_{SF} p_F \qquad \textbf{(2.139)}$$

And

$$f_S = -\rho_0 c_0^2 H_{SF}^T \ddot{d}_S \qquad \textbf{(2.140)}$$

The acoustic-structure problem can then be described by an unsymmetrical system of equations

$$\begin{bmatrix} M_S & 0 \\ \rho_0 c_0^2 H_{SF}^T & M_F \end{bmatrix} \begin{bmatrix} \ddot{d}_S \\ \ddot{p}_F \end{bmatrix} + \begin{bmatrix} K_S & -H_{SF} \\ 0 & K_F \end{bmatrix} \begin{bmatrix} d_S \\ p_F \end{bmatrix} = \begin{bmatrix} f_b \\ f_q \end{bmatrix} \qquad \textbf{(2.141)}$$

3. NUMERICAL ANALYSES

In this chapter, an overview of the numerical computations are given. The numerical simulations were performed with FEM solver Ansys Workbench R15.0. In the frame of this study, firstly each component which compose the freezer compartment was investigated individually. For this purpose, acoustic analysis of the freezer cavity and the modal analysis of the fan louver and evaporator cover were performed so the mode frequencies and mode shapes were obtained. Then to create a realistic model flow field inside the air duct was modeled and included to the analyses. In the last step, the coupled modal analysis was performed to solve the multi-physic problem between the structure and acoustic cavity. The change in the acoustic modes of the freezer cavity was observed.

Fluid-Structure Interaction (FSI) simulations are carried out using the multi-field solver, which employs implicit sequential coupling to calculate interactions between fluid and structural analysis. FSI techniques are used to compute effects between acoustic and structural domains using specialized acoustic elements as well.

In the detail of the analysis process, state variables were defined and the mathematical model was built up to describe the physical phenomena. The mathematical model may deviate from the real model due to various assumptions like viscosity and compressibility for fluid flow and stiffness and damping for structure.

3.1 Acoustic Modal Analysis of Freezer Cavity

The geometry of finite element model has been designed using PTC Creo Parametric 2.0 and then imported into Ansys Workbench R15.0 modal analysis module to perform acoustic analysis. The density of elements has been calculated using twenty elements per wavelength to give a maximum frequency of 654 Hz for which the model is valid. The accuracy of the results provided by a finite element model depends on the number and type of elements that are used to grid the volume of cavity. Experimental knowledge of the cavity is available, thus the results provided by the model can be compared to the results obtained experimentally, therefore making it possible to check the validity of the model. Furthermore, the results provided by the model can also be compared to the results calculated from theoretical model, cause of the shape of the cavity is similar to the rectangular box geometry. In this section, also theoretical results of the equivalent box model at the same outer size are presented. Figure 3.1 shows the studied freezer compartment of the refrigerator.

Figure 3.1 : Freezer compartment of the refrigerator.

The interior of a freezer compartment resembles a closed rectangular volume which has a simple analytical solution for its natural frequencies and acoustical modes.

The natural frequencies can be calculated from

$$f_{ijk} = \frac{c}{2}\sqrt{\left(\frac{i}{L_x}\right)^2 + \left(\frac{j}{L_y}\right)^2 + \left(\frac{k}{L_z}\right)^2}\,(\text{Hz}) \qquad \textbf{(3.1)}$$

And the mode shapes using

$$\Psi_{ijk} = cos\frac{i\pi x}{L_x} cos\frac{i\pi y}{L_y} cos\frac{k\pi z}{L_z} \qquad \textbf{(3.2)}$$

With $L_x = 0.661\, m$ and is the width of the freezer cabin, $L_y = 0.447\, m$ and is the height of the freezer cabin measured from bottom to top, $L_z = 0.446\, m$ and is the depth of the freezer cabin measured from the fan louver to the freezer door. The speed of sound, calculated at the room temperature (at *25º C*) and the indexes for normal modes of vibration $= 0,1,2, \ldots$, $j = 0,1,2, \ldots$, and $k = 0,1,2, \ldots$. Figure 3.2 shows the inner dimensions of the freezer compartment.

Figure 3.2 : Inner dimensions of freezer compartment.

Isometric 3D model for the freezer compartment is given in Figure 3.3.

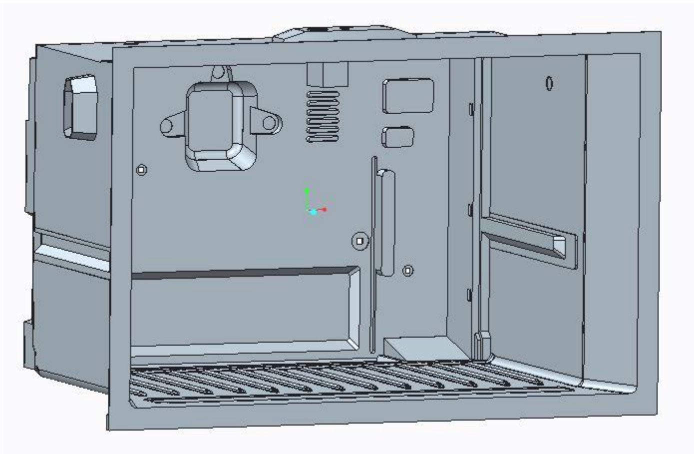

Figure 3.3 : Isometric 3D model of freezer compartment.

A convergence study on the number of elements has been performed to get better accuracy between the numerical and experimental model. A convergence study proceeded as follow: the acoustic modes of the cavity are computed for models with an increasing number of elements. Increasing the number of elements increase the accuracy of the model until a certain number of elements is reached, beyond this number accuracy does not improve much. The minimum number of elements to be used with satisfied accuracy. Figure 3.4 shows the meshed model of the freezer cavity.

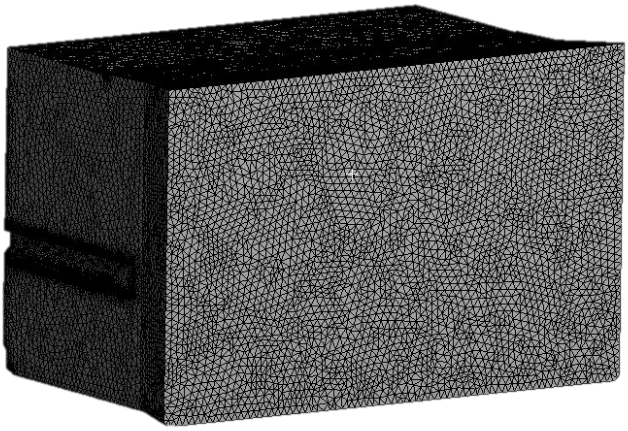

Figure 3.4 : Meshed model of the freezer cavity.

To define the acoustic model in simulation environment, the dimension of the cavity of freezer cabin and the characteristic of the fluid (air at 25º C) was entered; the natural frequencies and mode shapes were computed using Ansys Workbench R15.0, ACT Acoustic Extension Tool. Figure 3.5 shows the first ten natural frequencies of the freezer cavity, mode numbers and their index descriptions.

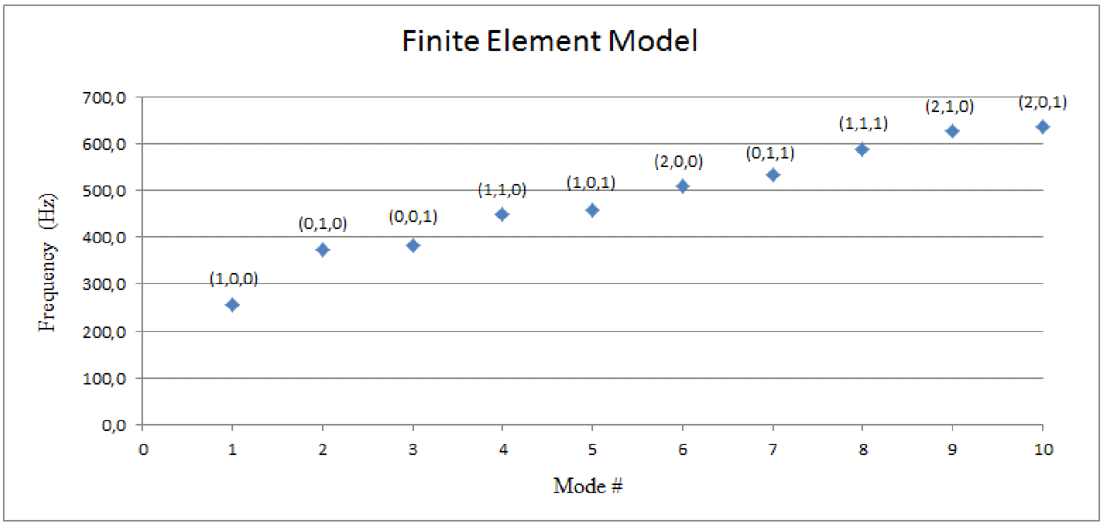

Figure 3.5 : First ten natural frequency of the freezer cavity.

The compared natural frequencies between analytical solution and numerical solution are presented in Table 3.1 and Figure 3.6 show the first three numerical acoustic mode shapes of the freezer cavity.

Table 3.1 : Comparison of analytical and numerical natural frequencies.

Mode	index i	index j	index k	Theory (Hz)	F.E. Model (Hz)	Difference (%)
1	1	0	0	255.2	259.4	1.6
2	0	1	0	373.6	383.7	2.5
3	0	0	1	381.7	384.5	0.7
4	1	1	0	448.4	463.2	3.2
5	1	0	1	457.9	463.9	1.3
6	2	0	0	509.5	518.9	1.8
7	0	1	1	533.0	543.2	1.9
8	1	1	1	587.4	602.0	2.4
9	2	1	0	627.0	645.4	2.5
10	2	0	1	635.1	645.8	1.7

The results obtained with the finite element model of the freezer cavity are closely matched to those obtained analytically from the rectangular box model. In terms of natural frequency, the largest difference occurs at 463.2 Hz where absolute difference is 14.8 Hz (3.2%). The main reason of this discrepancy is the minor geometrical differences among the models. At other frequencies, differences not exceed the ratio of (2.5%), and this shows that numerical model agrees very well with the analytical model.

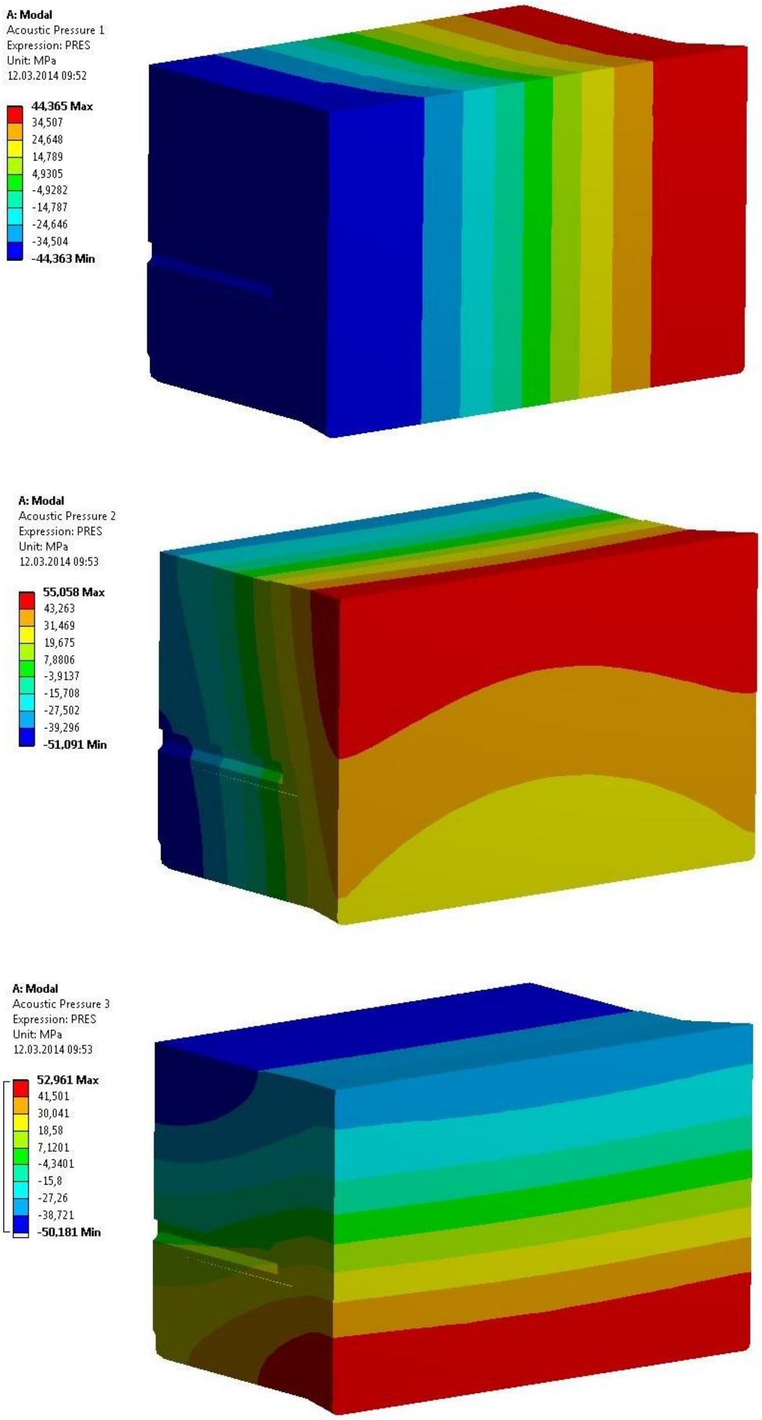

Figure 3.6 : First three acoustic mode shapes of freezer cavity.

3.2 Modal Analysis of Fan Louver and Evaporator Cover

In the household refrigerators, freezer air duct is composed of two components, fan louver and evaporator cover are shown in Figure 3.7 and Figure 3.8 respectively. The air, which is cooled by evaporator behind the freezer compartment, is blown by freezer fan unit and passes through air duct to freezer compartment. Evaporator cover has some ribs which lead air to the openings, called discharge holes, located on fan louver.

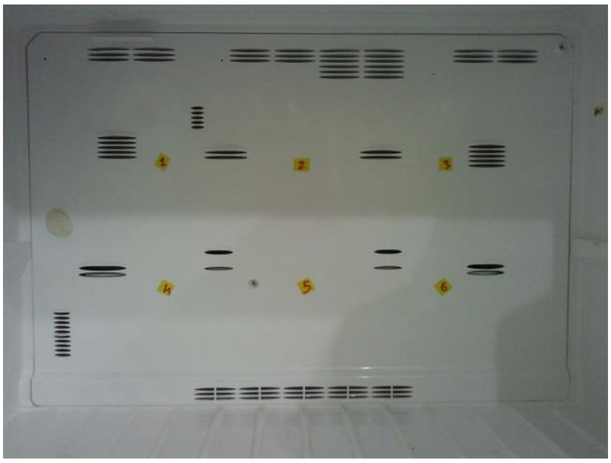

Figure 3.7 : Fan louver.

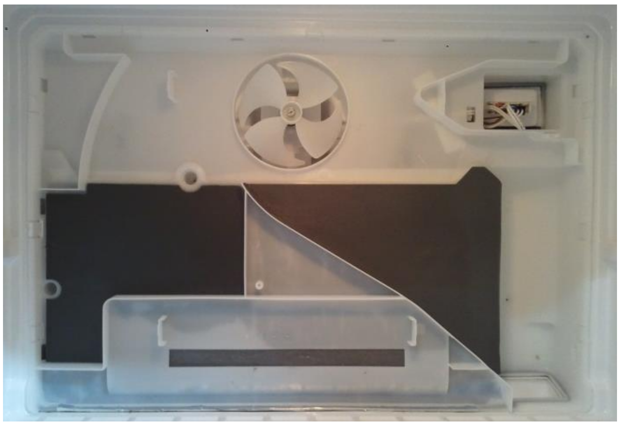

Figure 3.8 : Evaporator cover.

To identify natural frequencies and mode shape of air duct, three dimensional finite element analysis and simulation was carried out. In the numerical model, the evaporator cover and fan louver were modeled as coupled and flexible. Both of the components are made of polypropylene with the material properties are shown in Table 3.2.

Table 3.2 : Material properties of fan louver and evaporator cover.

Property	Fan Louver	Evaporator Cover
Density (kg/m^3)	932	4660
Young Modulus (Pa)	900000000	700000000
Poisson Ratio	0.42	0.30

The first ten natural frequencies of fan louver and evaporator cover calculated from the finite element models are listed in Table 3.3.

Table 3.3 : First ten natural frequencies of fan louver and evaporator cover.

Mode	Fan Louver (Hz)	Evaporator Cover (Hz)
#1	4.8	15.0
#2	36.5	18.3
#3	49.0	35.8
#4	54.6	58.8
#5	76.3	73.6
#6	105.1	80.5
#7	111.2	90.5
#8	130.6	103.5
#9	132.3	110.5
#10	150.2	117.0

3.3 Fluid Analysis of Air Cavity

Fluid field of air cavity was extracted from air duct and the numerical simulation of the fluid model has been created adding axial freezer fan driven by a motor rotating at 2200 rpm. The location of the axial fan inside the evaporator cover is given in Figure 3.9. The axial fan has 4 blades with outlet diameters of 100 mm and was located to the center of the air inlet hole.

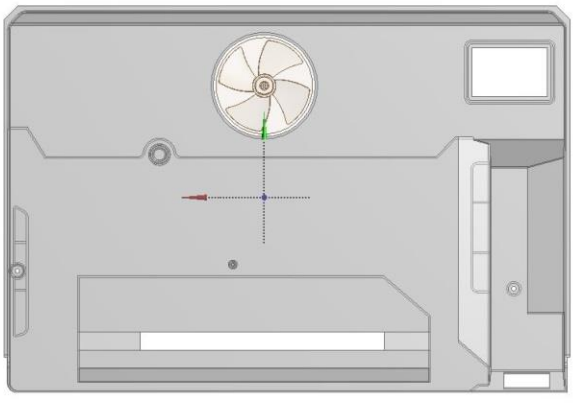

Figure 3.9 : The location of the axial fan inside the evaporator cover.

3.3.1 Numerical details

As boundary conditions, no-slip is defined at the walls, pressure inlet and pressure outlet. Pressure inlet boundary condition is used to define the fluid pressure at the air inlet hole and negative values are set to simulate the back pressure due to pressure loss of the system. Pressure inlet boundary condition is applicable for both incompressible and compressible flow calculations. Pressure inlet boundary condition can be used when the inlet pressure is known but the flow rate and/or velocity is not known.

Pressure outlet boundary conditions are defined for the discharge holes are located on fan louver. Operating pressure is set to normal working condition and a gauge pressure required in pressure outlet boundary condition specified as zero. The backflow conditions due to the reversed flow of air across the boundary are also defined. This operation minimizes the convergence errors during the iteration process. Figure 3.10 shows the isometric 3D model of air duct's cavity and Figure 3.11 shows the isometric 3D model of axial fan.

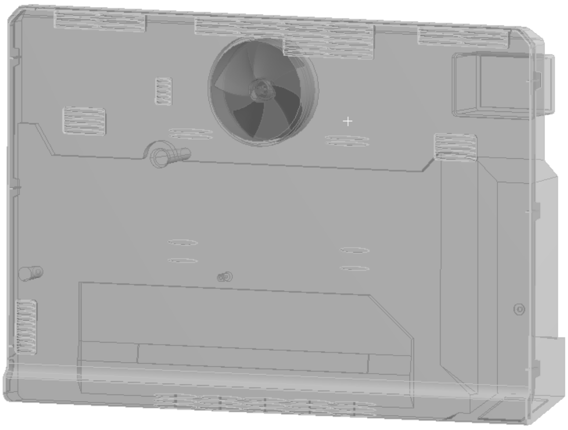

Figure 3.10 : Isometric 3D model of air duct cavity.

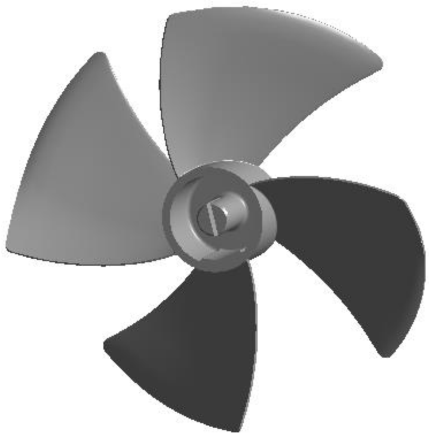

Figure 3.11 : Isometric 3D model of axial fan.

Using the finite volume method, flow domain is discretized into approximately 2.5 10^6 control volumes. The inflation method also applied on all of the surfaces of the cavity to resolve the boundary layer. A detailed view of the mesh for air duct's cavity and axial fan shown in the Figure 3.12 and Figure 3.13 respectively.

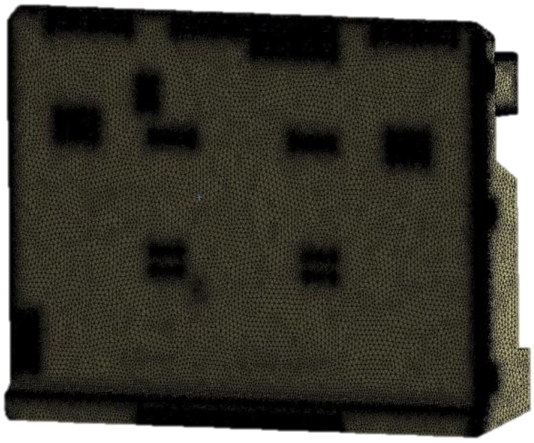

Figure 3.12 : Mesh model of air duct cavity.

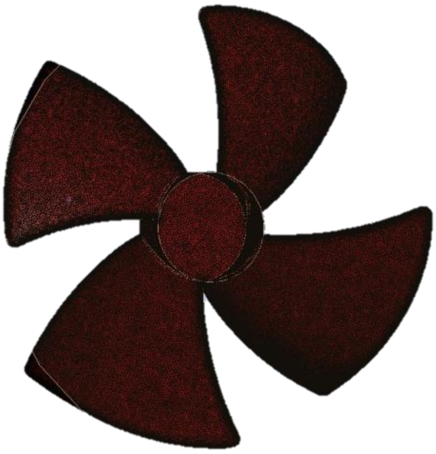

Figure 3.13 : Mesh model of axial fan.

Flow over propeller blades tends to cause asymmetries. In order to capture any possible asymmetries in the flow, the whole fan-duct geometry is simulated. Transition SST model is used to solve the flow field in the air duct. Spatial discretization is performed with the 2nd order upwind scheme.

Transition SST model is a variant of the standard $k-\omega$ model. Combines the original Wilcox $k-\omega$ model for use near walls and the standard $k-\varepsilon$ model away from walls using a blending function, and the eddy viscosity formulation is modified to account for the transport effects of the principle turbulent shear stress. This model especially preferred for the flows involving rotation, boundary layers under strong adverse pressure gradients and separation or recirculation.

3.3.2 Moving reference frames

In the created model, the fluid flow conditions were supplied by the rotation of the fan blades. To simulate this motion “moving reference frame” technique was used. In this approach, frame of reference is attached to the moving domain and governing equations are modified to account for this moving frame. Actually there is no moving part or mesh just the local accelerations are added as source terms to each grid cell. This technique provides a steady approximation of the interaction between the fan and the duct.

In this study, the simulations are performed in steady-state conditions with transition SST turbulence model. In transition SST model, four-transport equations are solved in addition to the RANS equations. This model provides better performance at capturing near wall behavior than two-equation $k-\varepsilon$ model and gives more stable solutions. This property is especially important in solving flow field around the blades.

The pressure-based coupled solver was used as a solution method. This method provides faster convergence than other methods. The computation was carried out with second order discretization method to obtain higher accuracy. The calculation of the solution was obtained after 250 iterations.

Figure 3.14 shows the streamlines of the velocity field of air cavity and Figure 3.15 shows the magnitude of the velocity at axial fan surface.

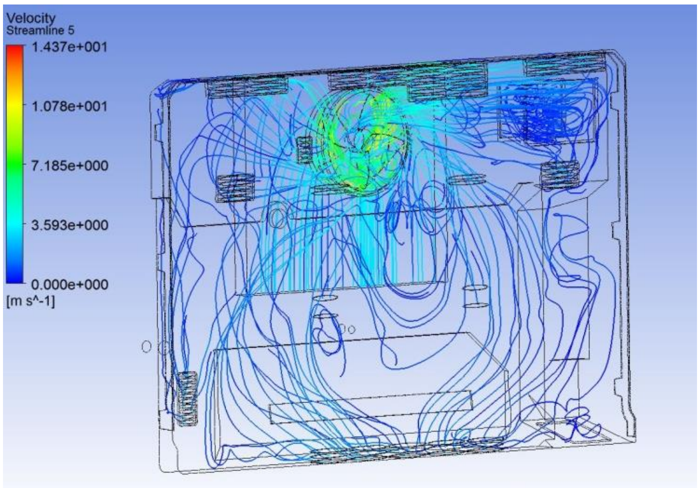

Figure 3.14 : Streamlines of the velocity field of air cavity.

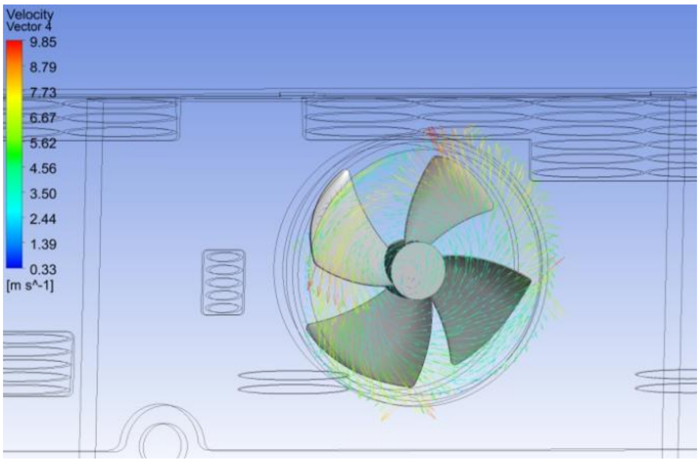

Figure 3.15 : Magnitude of the velocity at axial fan surface.

Figure 3.16 and Figure 3.17 shows the pressure distributions on front surface and rear surface of the cavity.

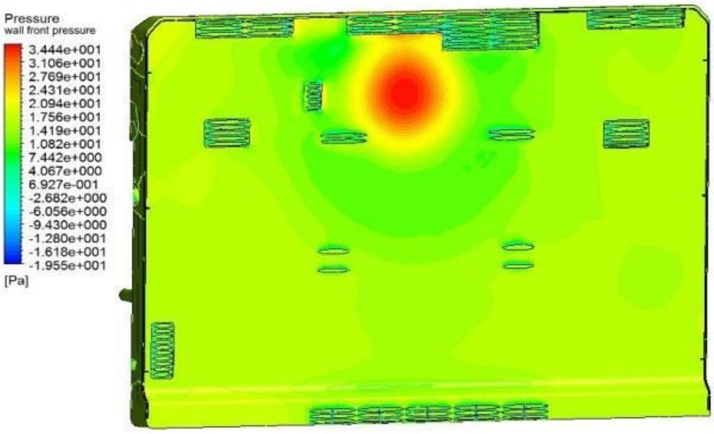

Figure 3.16 : Pressure distribution on front surface of the cavity.

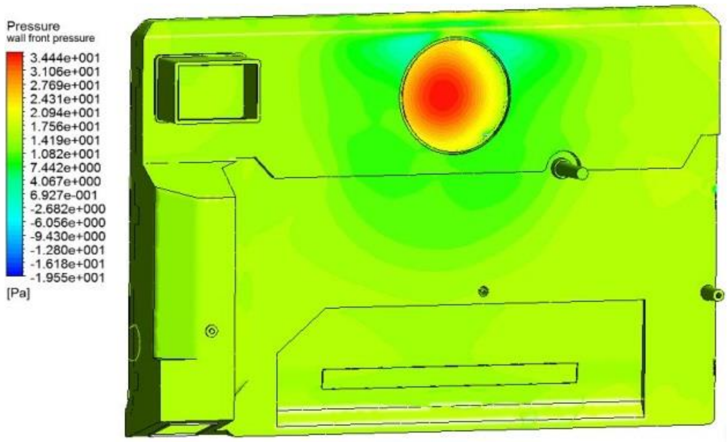

Figure 3.17 : Pressure distribution on rear surface of cavity.

3.4 The Fluid-Structure Interaction

Fluid-Structure Interaction (FSI) analysis is a multiphysic problem where the interaction between two different physics phenomena, done in separate analyses, is taken into account. In this study, response of a structure under the flow induced loads is investigated. The pressure loads coming from CFD analysis of the cavity are imported to the corresponding structural analysis of the fan louver. This interaction is taken at the boundaries that fluid domain shares with the structural domain commonly. The results of the CFD analysis are applied to the structural analysis as an initial condition.

The partitioned approach is used for the simulation of fluid-structure interaction. In this approach, the equations governing the flow and the displacement of the structure are solved separately with two distinct solvers. In this study, primarily CFD analysis is performed and then structural analysis is performed by force of this approach. This means that the flow does not change while the structural solution is calculated. The results are interpolated to structural analysis after the completion of the CFD analysis.

In this approach, the information is exchanged at the interface between two solvers, this process is defined as the “coupling”. Figure 3.18 shows the algorithm of the partitioned approach.

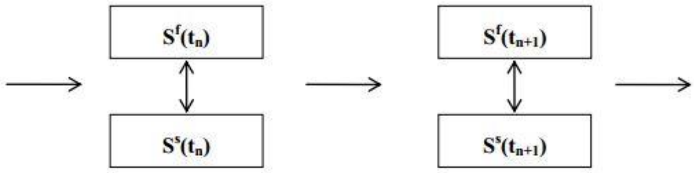

Figure 3.18 : Algorithm of the partitioned approach.

One-way coupling method is carried out to transfer the data from fluid analysis to structural analysis. In this method, the motion of a fluid flow influences a solid structure but the reaction of a solid upon a fluid is negligible. The resulting forces at the interface from fluid calculation of the cavity are interpolated to the structural mesh of the fan louver. Then the static structural analysis is performed. Figure 3.19 shows the direct project schematic connection among the analyses.

Figure 3.19 : The direct project schematic connection.

Fluid Structure Interaction also can be categorized by the degree of physical coupling between the fluid and solid solution fields. The degree of this coupling specifies that how one field is sensitive to a changing in the other field. Fields that are strongly coupled physically require strong numerical coupling and solution is generally more difficult. In this study, coupling degree is weak cause of the physical shape of the geometries thus the sensitivity is less than the strongly coupled systems.

3.4.1 Data transfer

Data transfer between the coupled participants is one of the critical parts of an FSI analysis. In our study, static load transfer method was used in accordance with the nature of the coupling method. In details of this data transfer method, the information is exchanged between two different meshes of different mediums at the interface of these mediums. This is carried out by a systematic sequence. The first process of the data transfer is to match or pair the source and target mesh to generate weights. The source mesh feeds the data to the target mesh and this matching is done by using the *General Grid Interface* mapping algorithm. The conservative nature of *General Grid Interface* algorithm is shown in Figure 3.20. This method is just available in one-way coupling.

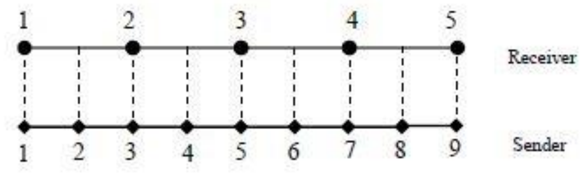

Figure 3.20 : General grid interface.

3.4.2 Imported boundary conditions

Using the FSI capabilities of ANSYS, the pressure distribution obtained from fluid analysis on front and back side of the air duct transferred to the structural analysis as boundary conditions. Figure 3.21 and Figure 3.22 respectively shows the pressure load imported to the fan louver and evaporator cover as an initial condition.

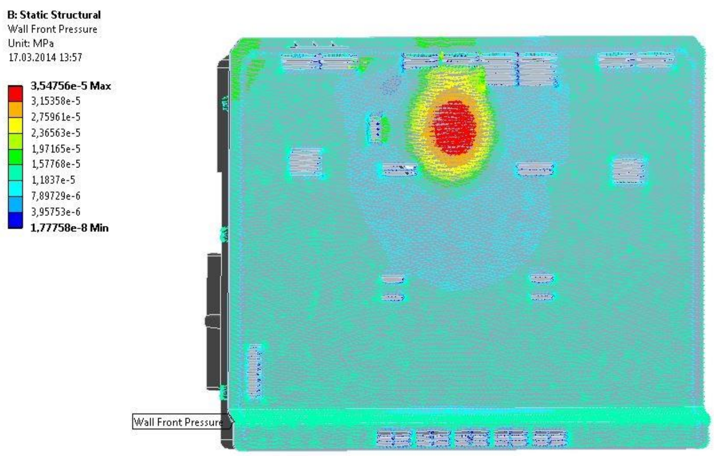

Figure 3.21 : Pressure load imported to the fan louver.

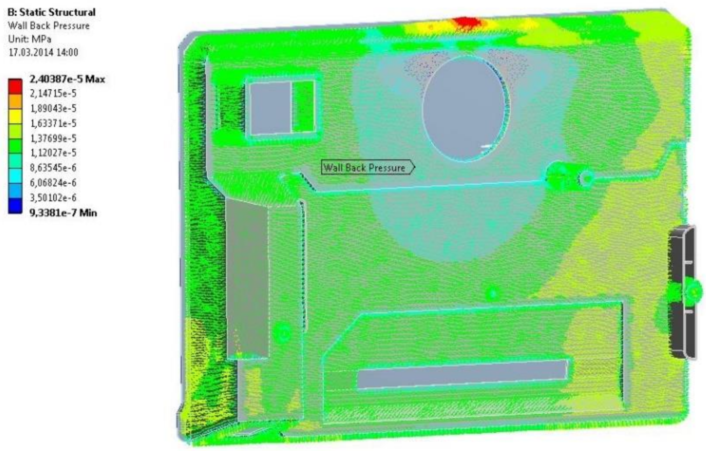

Figure 3.22 : Pressure load imported to the evaporator cover.

3.5 Structural Analysis of Fan Louver

In structural analysis of fan louver, primarily solution set-up was prepared. The contact surfaces were assigned as a bonded between target surface and body surface. As an initial condition, fixed supports were defined at the surrounding frame of the evaporator cover to reflect the real conditions in freezer cabinet and the imported pressure distribution results from the fluid analysis was applied as a load at inner surface of the fan louver. Figure 3.23 shows the contact surfaces on fan louver and evaporator cover.

Figure 3.23 : Contact surfaces on fan louver and evaporator cover.

In step of analysis setting, “large deflection” option is set to on. For simple linear static analyses which deflection and strain is small, this option typically is set to “off” if the displacements are small enough that the resulting stiffness changes are insignificant. But in our case to obtain more accurate results in a pre-stress modal analysis will be generate at next step, this option must open in this static structural analysis cause of the deformation in modal analysis is high.

Setting "large deflection" to on, opens the geometric nonlinearities and will take into account stiffness changes resulting from changes in element shape and orientation due to large deflection, large rotation and large strain. Therefore the results give more accurate solutions. However this effect requires an iterative solution. In addition it also needs the load to be applied in small increment. Therefore, the solution takes longer time.

In analysis settings, a pressure load was applied at 10 steps with a time step of 0,1 second between each iteration starting at time 0. Figure 3.24 shows the vector principle stress distribution on fan louver.

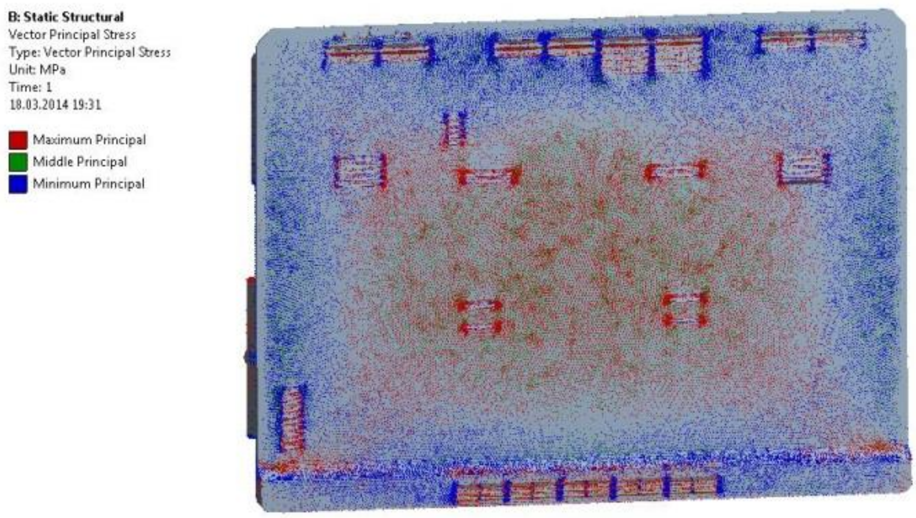

Figure 3.24 : Vector principle stress distribution on fan louver.

3.6 Coupled Acoustic-Structure Analysis of Fan Louver and Freezer Cavity

In this section, freezer cavity has been modeled and coupled with the solved pre-stressed structural analysis of fan louver. These two different domains were solved in same modal module. Figure 3.25 shows the direct project schematic connection among the modules.

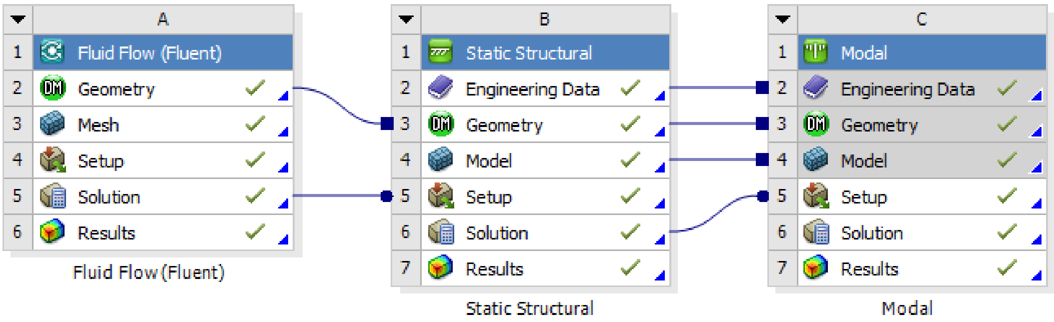

Figure 3.25 : The direct project schematic connection.

Freezer cavity was defined as acoustic body. Property of air was shown in Table 3.4. Reference pressure was taken as $20 \times 10^{-6} N/m^2$.

Table 3.4 : Material properties of freezer cavity.

Property	Freezer Cavity
Density (kg/m^3)	1.38
Speed of Sound (m/s) @25° C	346.13

Figure 3.26 shows the isometric 3D model of the coupled fan louver and freezer cavity.

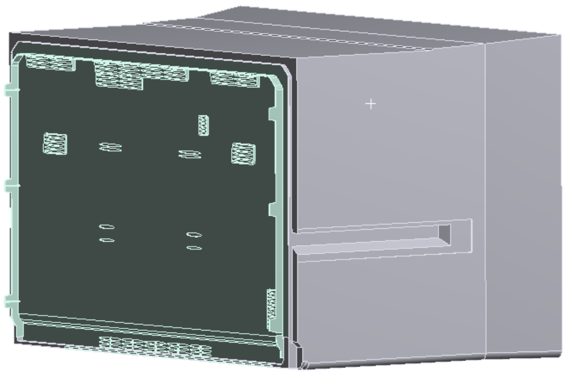

Figure 3.26 : Isometric 3D model of the coupled fan louver and freezer cavity.

For freezer cavity, frequency domain acoustics is governed by Helmholtz equation for the acoustic pressure, *p*.

$$\nabla.\left(-\frac{1}{\rho_o}\nabla p\right) - \frac{\omega^2}{\rho_o c^2} p = 0\,, \omega = 2\pi f \tag{3.3}$$

A coupled acoustic analysis also takes the fluid-structure interaction into account. The governing equation for acoustics has been discretized taking into account the coupling of acoustic pressure and structural motion at the interface. Specifying the acoustic FSI label couples the structural motion and fluid pressure at the interface. Acoustic elements used in freezer cavity have the capabilities to translate pressure at non-fluid medium and the translations in x, y, z directions at the interface.

The dissipative effects due to fluid viscosity and the absorption resulting from damping are neglected. The boundaries enclosing the acoustic cavity are assumed as hard and hence the pressure gradients on all boundaries without FSI interface are set to zero. Before generating the analysis, all openings upon fan louver were closed to fulfill the requirements of acoustic FSI at the interface.

Table 3.5 shows the compared first ten natural frequencies of the freezer cavity both coupled and uncoupled with fan louver.

Table 3.5 : First ten natural frequencies of freezer cavity coupled and uncoupled.

Mode	Uncoupled Freezer Cavity (Hz)	Coupled Freezer Cavity (Hz)
#1	259.4	262.6
#2	383.7	386.7
#3	384.5	388.3
#4	463.2	468.7
#5	463.9	469.9
#6	518.9	526.1
#7	543.2	551.8
#8	602.0	613.0
#9	645.4	657.6
#10	645.8	658.7

When the obtained results are compared, it is obviously seen that the impact of the fan louver over the freezer cavity increases the natural frequency of the freezer cavity. These differences increase in higher frequencies approximately (2%). But there is almost never change in mode shapes of the freezer cavity, in comparison to uncoupled results of freezer cavity.

Figure 3.27 shows the first three mode shapes of freezer cavity coupled with fan louver calculated from the finite element model.

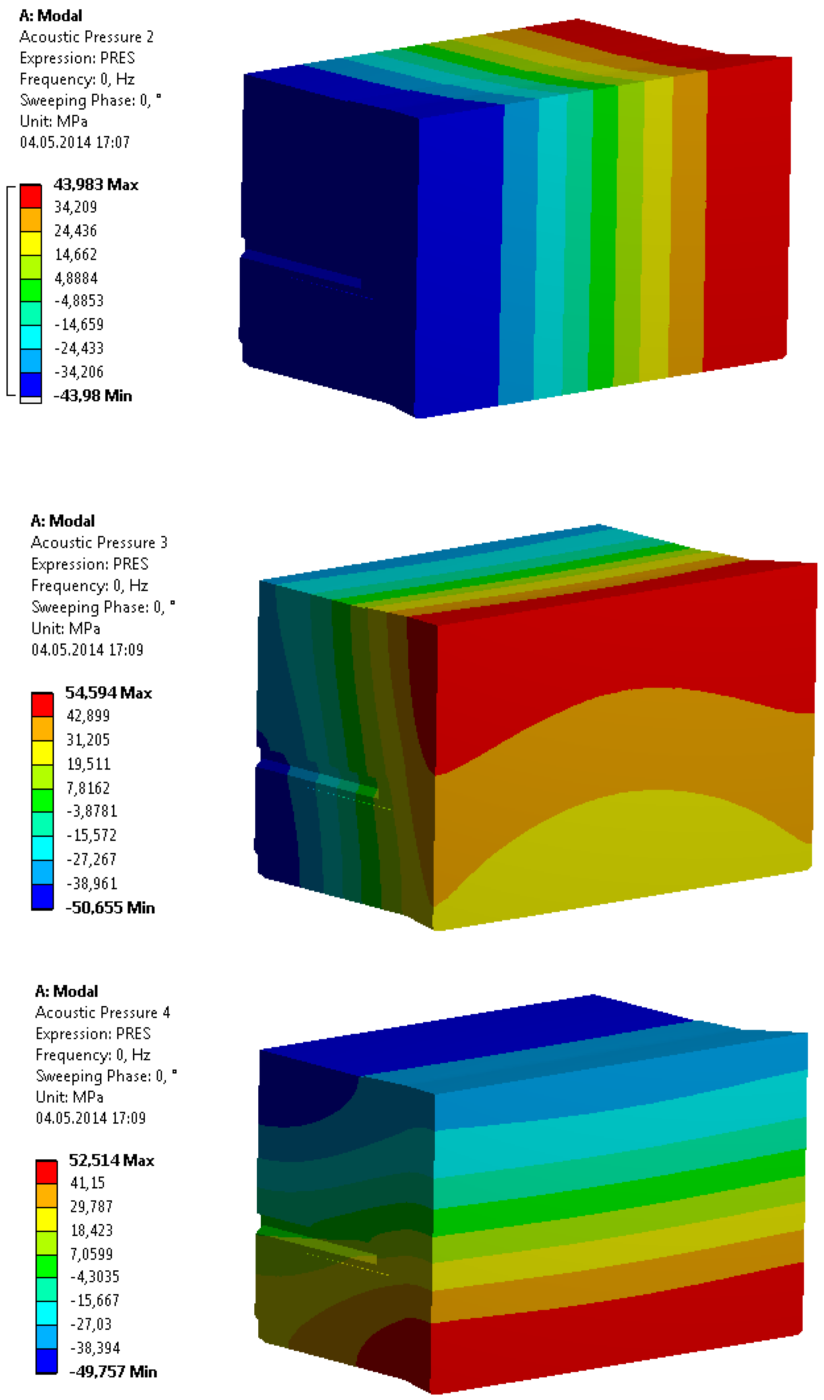

Figure 3.27 : First three acoustic mode shapes of freezer cavity coupled with fan louver.

4. EXPERIMENTAL ANALYSES

In this chapter, experimental measurements were performed to validate the numerical model. For this purpose, experimental acoustic modal analysis for the freezer cavity and modal analysis for the fan louver and evaporator cover were carried out. All data acquisition process was achieved by using the product Vestel No-Frost Refrigerator. Figure 4.1 shows the picture of the studied refrigerator.

Figure 4.1 : The studied refrigerator.

4.1 Experimental Acoustic Modal Analysis of Freezer Cavity

Three modal parameters that can be extracted from the experimental modal analysis fully describe the dynamics of the cavity:

- Natural Frequencies (ω_n)
- Modal Damping Ratios (ζ_n)
- Mode Shapes (Φ)

These parameters also be obtained analytically with the knowledge of the dimensions, the shape and boundary conditions of the freezer cavity. However, analytically obtained damping associated with each mode is not straightforward. The algorithm used to extract these parameters is based on a frequency domain curve fitting of the transfer function $H(\omega)$ between the pressure measured at point i inside the cavity and the pressure measured at point k location of the speaker used to create the pressure field. The transfer function can be expressed by modal superposition, in terms of the modal parameters:

$$H(\omega) = \frac{P_i}{P_k}(\omega) = \sum_{i=1}^{m} \frac{\Phi_{im}\Phi_{km}}{M_m(\omega_m^2 - \omega^2 + 2\zeta_m \omega \omega_m)} \quad \textbf{(4.1)}$$

Where M_m is the modal mass, ω_m is the natural frequency, ζ_m is the damping of mode m and Φ_{im} is the modal participation of mode m at point i. The mode shapes are proportional to the modal participation:

$$\begin{Bmatrix} modeshape_m\ (x_1) \\ \cdots \\ modeshape_m\ (x_k) \\ \cdots \end{Bmatrix} = \alpha_m \begin{bmatrix} \Phi_{m1}\Phi_{mk} \\ \cdots \\ \Phi_{mk}\Phi_{mk} \\ \cdots \end{bmatrix} \quad \textbf{(4.2)}$$

Where α_m is the coefficient of proportionality for the mode m.

The system presented in Figure 4.2 is used to perform the acoustic modal analysis.

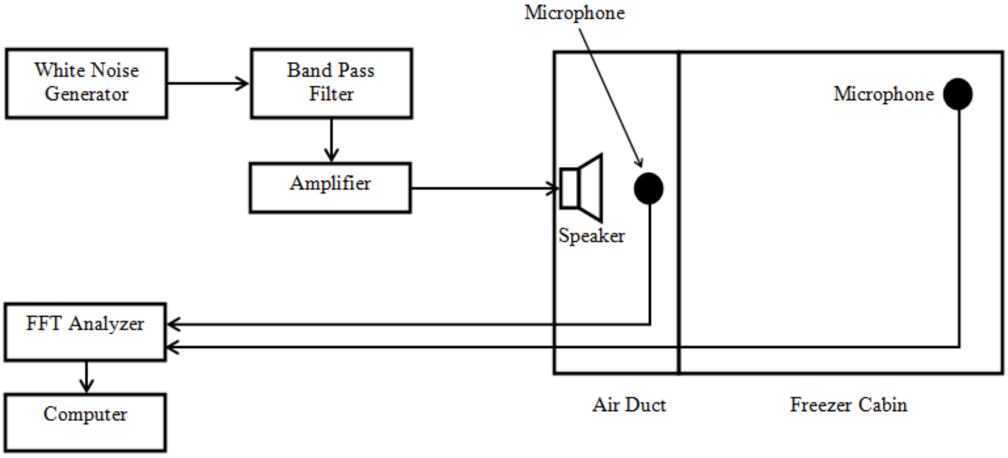

Figure 4.2 : Acoustic modal analysis system configuration.

The signal from a white noise generator is limited between 0 and 1250 Hz and an amplifier is used to adjust the level of the signal received by loudspeaker to acoustically excite the freezer cavity. The loudspeaker was located to the place of the axial fan at the center of the air inlet hole inside the air duct and isolated from the evaporator cover with soft foam. Figure 4.3 shows the positions of the loudspeaker and reference microphone.

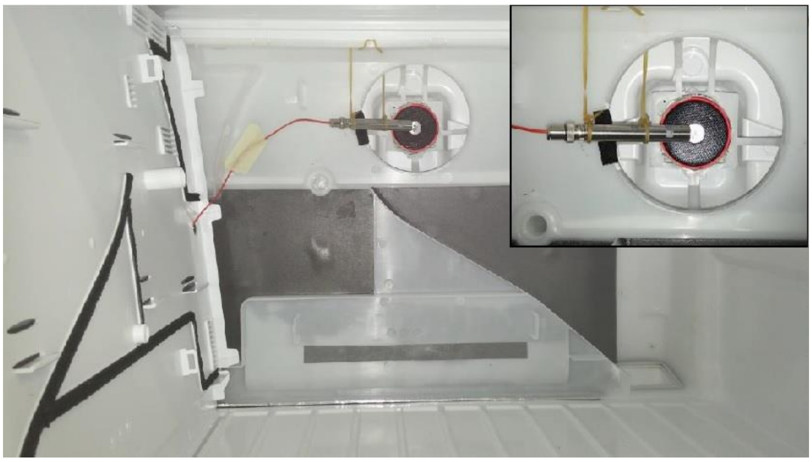

Figure 4.3 : Position of the loudspeaker and reference microphone.

Before the measurement, entire accessories like ice tray and glass shelf were removed. The acoustic pressure measurement was performed in total 12 points on four rows with three different microphone positions inside the freezer cavity. Figure 4.4 shows four rows of the microphone positions.

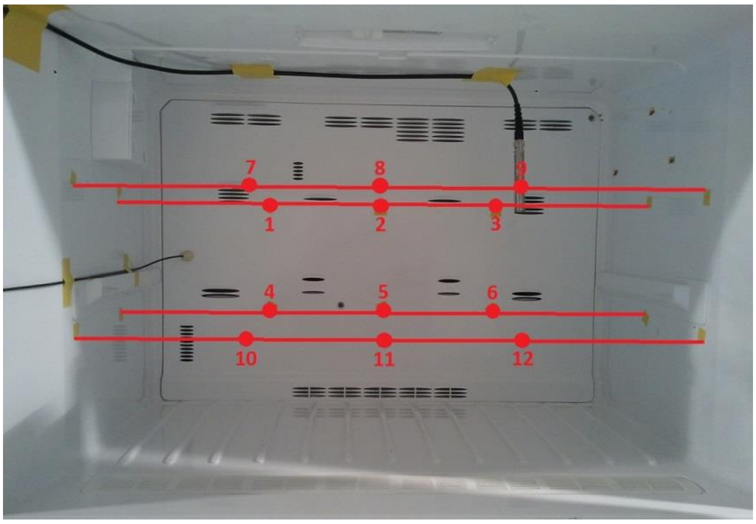

Figure 4.4 : Four rows of the microphone positions.

The signals were acquired by GRAS 46AE ½” free-field microphones with a 4 channel FFT analyzer linked to a computer for post processing. Two microphones were used at one measurement, one microphone which is located close to the sound source was used as a reference signal and one microphone which is located inside the freezer cavity was used as a response signal. The acquisition processes were repeated 12 times for each measuring position. The FFT analyzer computes the autospectrum of each channel as well as the cross spectrum between the reference microphone connected to channel 1 and the response microphone connected to channel 2. This information is required for computation of both the transfer function H_1 and the coherence v. The frequency response function between microphones responses at all the grid points with respect to the reference microphone was measured. (Pa/Pa)

$$\mathrm{H}_1 = \frac{G_{xx}G_{yy}}{G_{xy}} \quad \textbf{(4.3)}$$

$$v = \frac{{G_{xy}}^2}{G_{xx}*G_{yy}} \quad \textbf{(4.4)}$$

In measurement set-up, data was collected during 10 seconds for each point with taking the linear average of the signal. Frequency resolution was set to 1,563 Hz between frequency ranges of 0 – 1250 Hz. In order to satisfy the better periodicity requirement of the FFT analysis, Hanning weighting function was used. This function also minimizes the leakage error.

All measurements were taken at the room temperature (25°C) inside the semi-anechoic room. Figure 4.5 shows the picture of the semi-anechoic room.

Figure 4.5 : The semi-anechoic room.

Figure 4.6 through Figure 4.9 shows the frequency response spectrum of all four measurement rows.

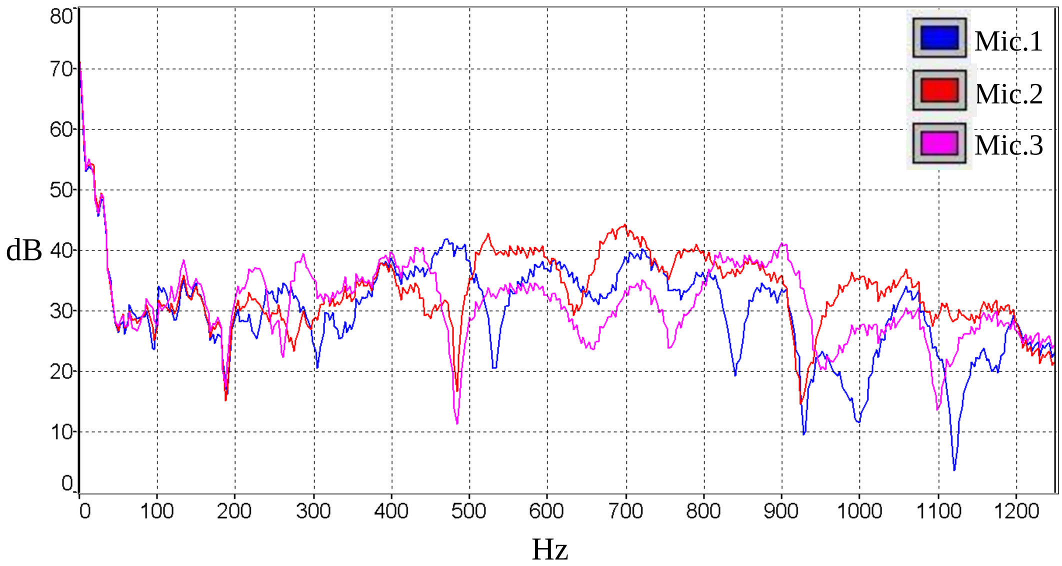

Figure 4.6 : Frequency response spectrum (upper rear row).

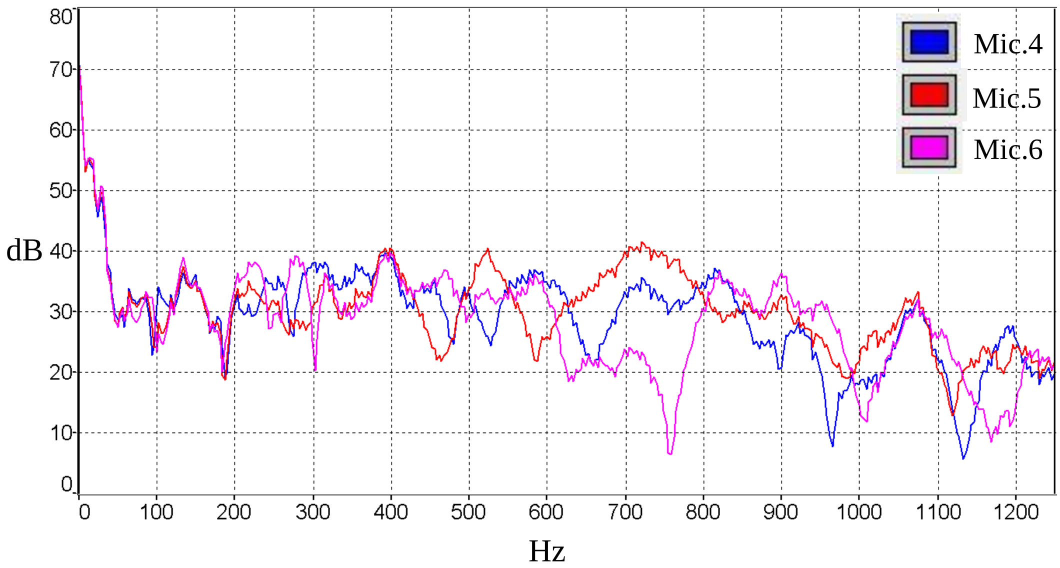

Figure 4.7 : Frequency response spectrum (lower rear row).

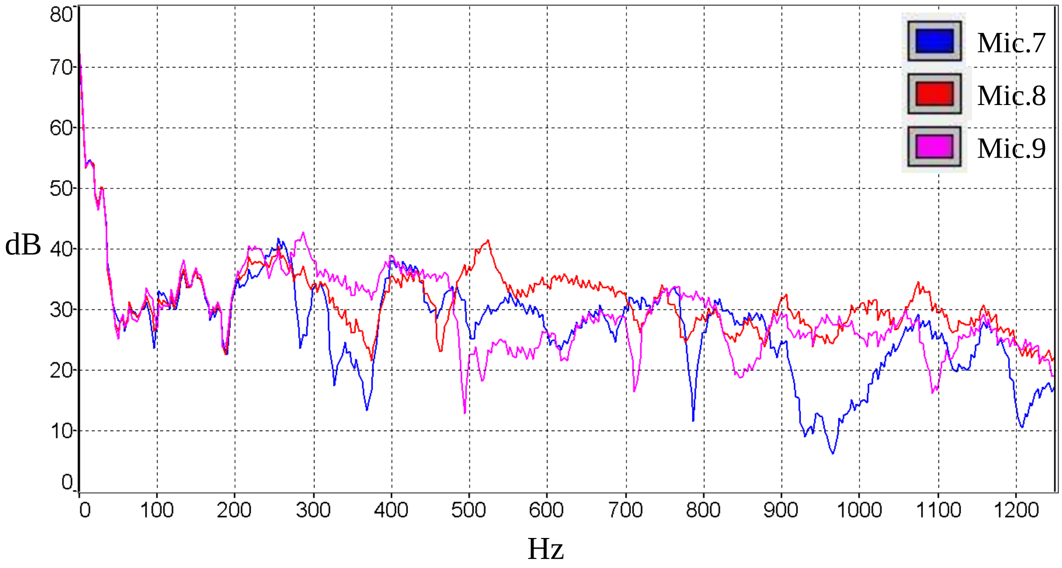

Figure 4.8 : Frequency response spectrum (upper front row).

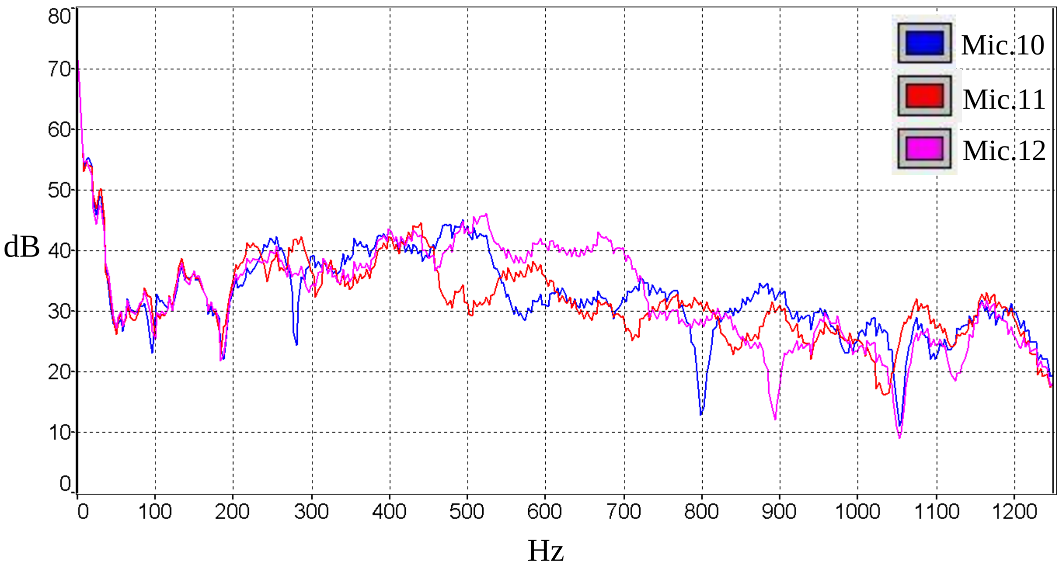

Figure 4.9 : Frequency response spectrum (lower front row).

From the analytical solution, we know the frequency interval which we have to investigate. Analytical results show that the first ten modes of the freezer cavity is between frequency ranges of 250 - 650 Hz. The measured first ten natural frequencies of freezer cavity are presented in Table 4.1.

Table 4.1 : The measured first ten natural frequencies of freezer cavity.

Natural Frequencies (250-650 Hz) Experiment
261.4
381.4
384.3
454.2
462.3
531.8
554.7
619.0
662.1
664.3

On the other hand, when the frequency response spectrum was investigated, some peak frequencies are also seen between frequency ranges of 0 - 250 Hz. Generally, these lower peak values could not be belong to modes of the cavity cause of the dimensions of the cavity. The main reason of this phenomenon could be the structural born noise which is radiated from the vibration of the air duct. Because of that, these lower peak frequencies are clearly seen at all measurement points. In this reason, the dynamic behavior of the air duct also analyzed within the scope of this study. Table 4.2 shows the measured peak frequencies obtained from the experiments between the intervals of 0 - 250 Hz.

Table 4.2 : The measured peak frequencies.

Peak Frequencies (0-250 Hz) Experiment
31.2
56.2
65.6
87.5
103.1
118.7
134.3
150.0
178.1
203.1

4.2 Experimental Modal Analysis of Fan Louver and Evaporator Cover

In this section, experimental modal analysis was applied to the air duct to define the dynamic characteristic of the structure under external load. A series of frequency response functions were measured at various geometric locations using an instrumented impact hammer to supply an input force. Responses are measured in the z direction with motion sensor, typically accelerometer. The system presented in Figure 4.10 is used to perform the modal analysis.

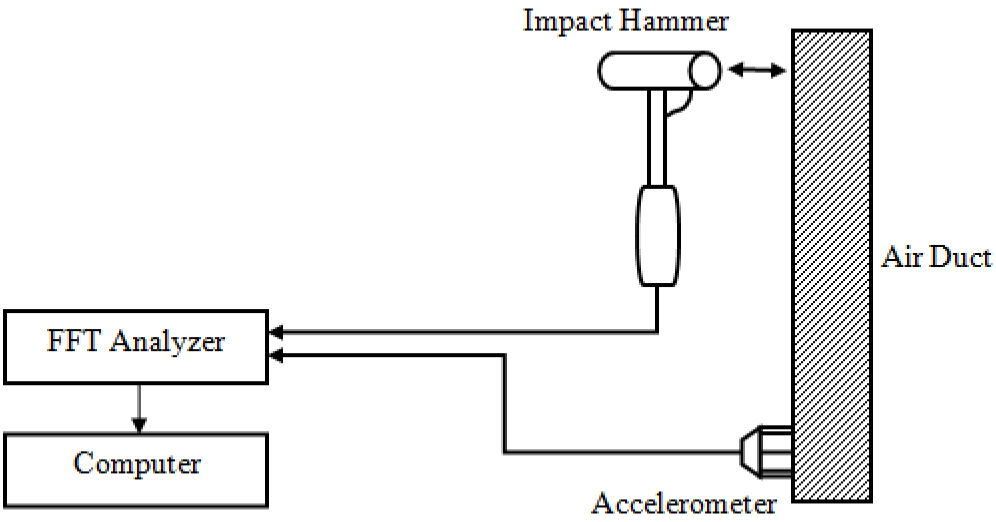

Figure 4.10 : Modal analysis system configuration.

The air duct composes of two separate components, one is the evaporator cover and the other one is fan louver. These two components were analyzed individually. The evaporator cover and fan louver were suspended with elastic cords from two points to simulate free – free conditions as close as possible. The measurements were taken from 84 points for evaporator cover and from 103 points for fan louver. Figure 4.11 shows the points where measurements were taken.

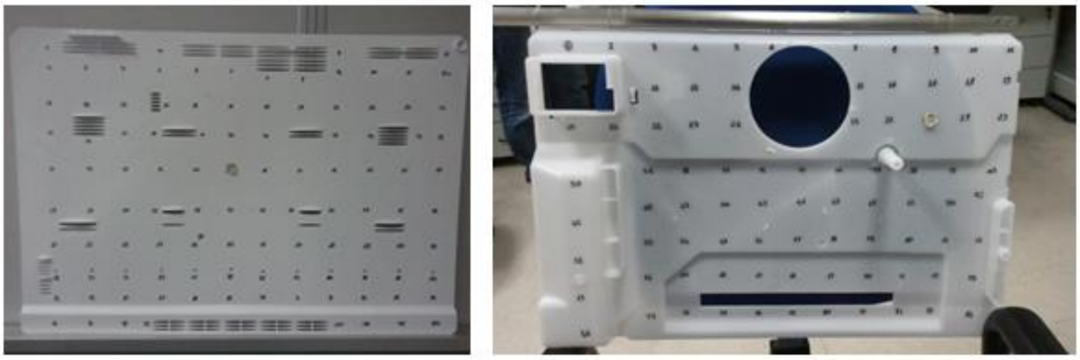

Figure 4.11 : Measurement points on fan louver and evaporator cover.

The experiment was performed with 4ch. FFT analyzer, one channel was used to acquire the force signal and one channel for acceleration signal simultaneously. Frequency response functions were measured between 0 and 250 Hz, using a frequency resolution of 0.78 Hz. The excitation was given in the horizontal direction by an impact hammer from one point and the response was measured at all defined points. A rubber tip impact hammer was used to provide a long pulse and excite a narrow frequency range.

In order to prevent the incorrect estimation of the amplitude and frequency due to the effect of the non-periodic signals, measurement period was extended and to better satisfy the periodicity requirement of FFT process, Hanning time weighting function was applied. This function attempts to heavily weight the beginning and end of the sample record to zero.

Table 4.3 shows the experimentally measured ten natural frequencies and the corresponding damping ratios of the fan louver and evaporator cover respectively.

Table 4.3 : The measured first ten natural frequencies and damping ratios of fan louver and evaporator cover.

Natural Frequencies (Hz)			
Fan Louver		Evaporator Cover	
Hz	%	Hz	%
5.0	2.1	14.1	2.6
37.0	2.4	18.8	1.7
46.5	1.5	32.8	3.1
55.5	2.5	56.3	2.2
77.0	0.8	70.3	2.7
104.0	1.3	79.7	1.3
112.0	2.4	89.8	3.0
129.0	4.1	101.0	3.2
133.0	2.9	107.0	1.9
149.0	3.1	114.0	3.1

When the results are investigated, a common inference could be made; the modal density is higher above 100 Hz for the both structures. There are five modes for the fan louver between 100 - 150 Hz and three modes for the evaporator cover between 100 - 115 Hz. The modal damping ratios obtained from the curve fitting algorithm by using the modal animation software ME’scope were also entered in numerical analyses.

5. EVALUATION OF THE RESULTS

In this chapter, to ensure the accuracy of the numerical model, the natural frequencies and mode shapes were compared with those measured experimental data for validation process. In the experimental analyses, the modal animation software ME'scope was used for the visualization of the mode shapes. In order to solve the interaction between the air duct and freezer cavity, overlapping frequencies were identified and design optimization process was performed to change the natural frequencies of the structure thus the interaction among the domains was reduced.

5.1 Comparison of Numerical and Experimental Results

The comparison of the first ten natural frequencies obtained from the numerical and experimental analysis for fan louver was given in Table 5.1.

Table 5.1 : The comparison of numerical and experimental natural frequencies for fan louver.

Modal Parameters of Fan Louver	
Natural Frequencies (Hz)	
Numerical Model	Experiment
4.8	5.0
36.5	37.0
49.0	46.5
54.6	55.5
76.3	77.0
105.1	104.0
111.2	112.0
130.6	129.0
132.3	133.0
150.2	149.0

Figure 5.1 shows the numerically and experimentally compared first three mode shapes of fan louver.

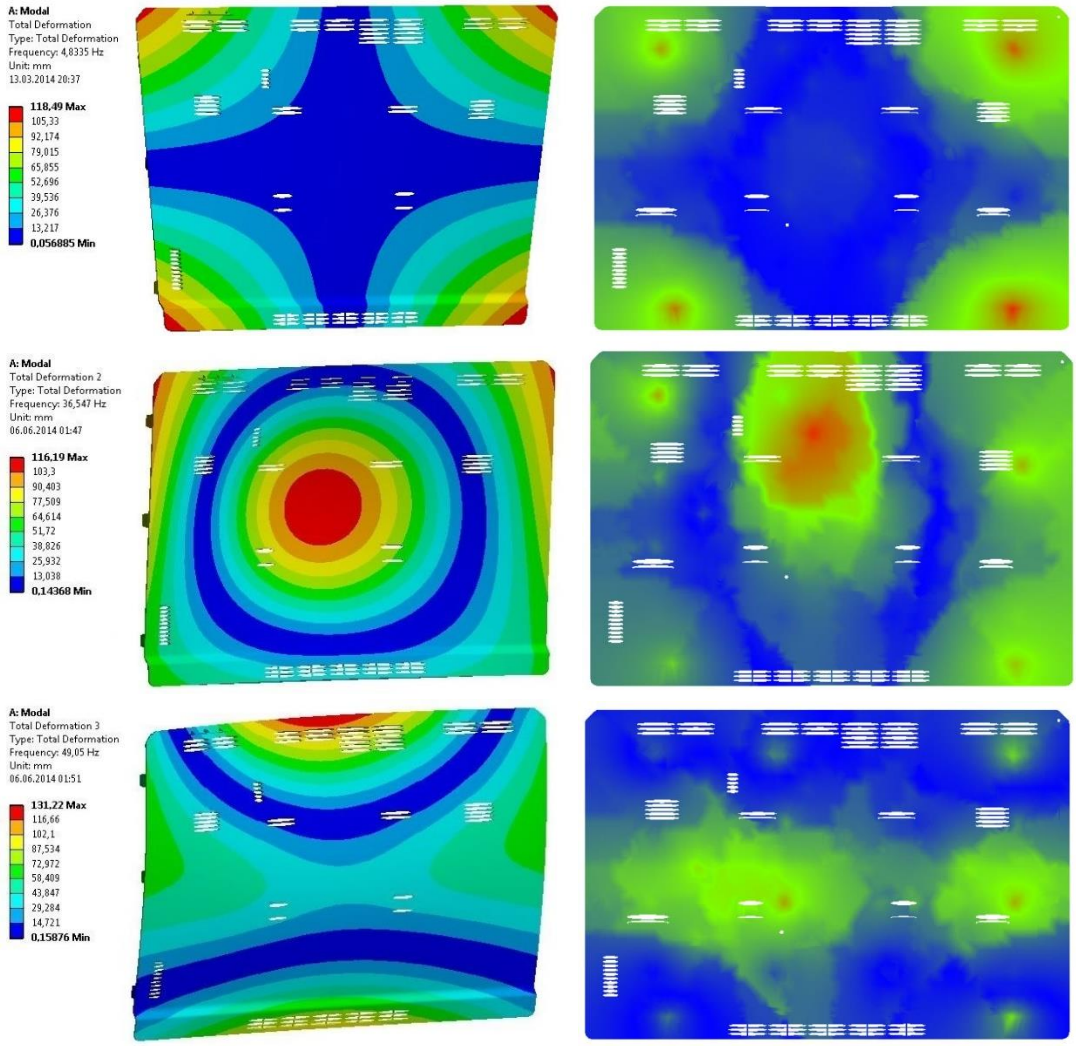

Figure 5.1 : The numerical and experimental comparison of the first three mode shapes of fan louver.

As can be seen in Table 5.1, the mode frequencies which are acquired from experimental analysis agreed rather well with those existing modes were obtained from numerical model of the fan louver. Although the used material polypropylene is highly damped, the experimental mode shapes of the fan louver can be seen obviously. Especially in third mode also some local mode shapes have even seen a little.

The comparison of the first ten natural frequencies obtained from the numerical and experimental analysis for evaporator cover was given in Table 5.2.

Table 5.2 : The comparison of numerical and experimental natural frequencies for evaporator cover.

Modal Parameters of Evaporator Cover	
Natural Frequencies (Hz)	
Numerical Model	Experiment
15.0	14.1
18.3	18.8
35.8	32.8
58.8	56.3
73.6	70.3
80.5	79.7
90.5	89.8
103.5	101.0
110.5	107.0
117.0	114.0

Figure 5.2 shows the numerically and experimentally compared first three mode shapes of evaporator cover.

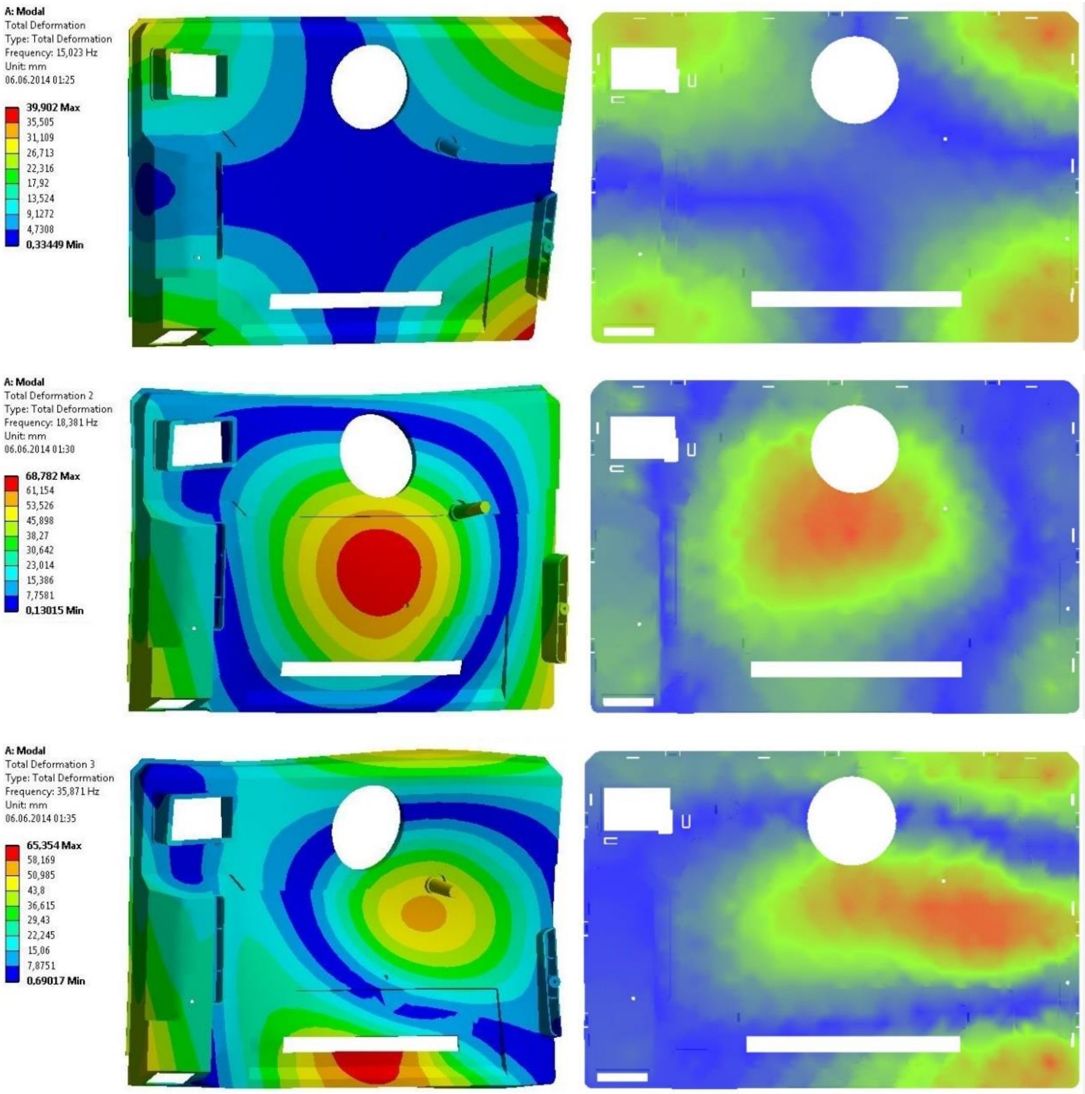

Figure 5.2 : The numerical and experimental comparison of the first three mode shapes of evaporator cover.

In Table 5.2, the mode frequencies obtained from the experimental measurements are closely matched with the natural frequencies obtained from the numerical model of the evaporator cover. Despite of the complexity of the geometry, acquired data clearly reflect the motion of the structure in Figure 5.2. Experimental mode shapes agree with the numerical mode shapes very well.

The numerical and experimental acoustic modes of the freezer cavity are presented in Table 5.3.

Table 5.3 : The comparison of numerical and experimental natural frequencies for freezer cavity.

Modal Parameters of Freezer Cavity	
Natural Frequencies (Hz)	
Numerical Model	Experiment
262.6	261.4
386.7	381.4
388.3	384.3
468.7	454.2
469.9	462.3
526.1	531.8
551.8	554.7
613.0	619.0
657.6	662.1
658.7	664.3

Between the interval of 261.4 Hz and 462.3 Hz, experimentally obtained modes are lower than the numerically obtained modes. Above that interval, experimental mode frequencies are beginning to diverge from the numerical mode frequencies.

Figure 5.3 shows the pressure distributions corresponding the first three acoustic modes inside the freezer cavity.

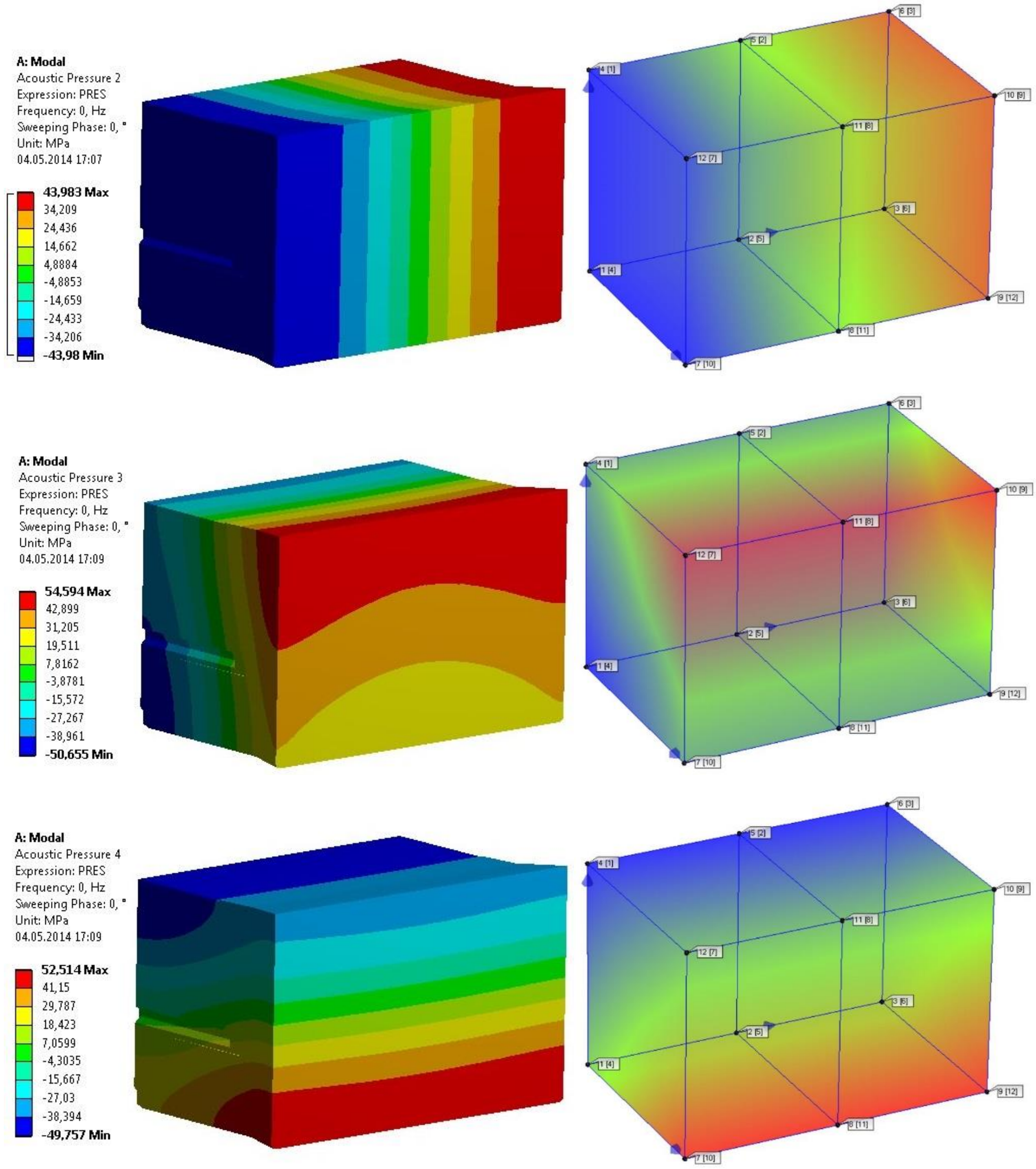

Figure 5.3 : The numerical and experimental comparison of the first three acoustic mode shapes of freezer cavity.

5.2 Design Optimization

In addition to acquired frequency response data inside the freezer compartment, the sound pressure data also collected in normal working condition of the refrigerator. The measurement was performed when the freezer fun is running and the sound pressure vs frequency spectrum data was collected by one microphone. The rotational speed of the freezer fan is 2200rpm and the blade passing frequency is 147 Hz for the impeller with four blades. From Figure 5.4 the blade passing frequency (147 Hz) and its second harmonic (294 Hz) can be seen easily.

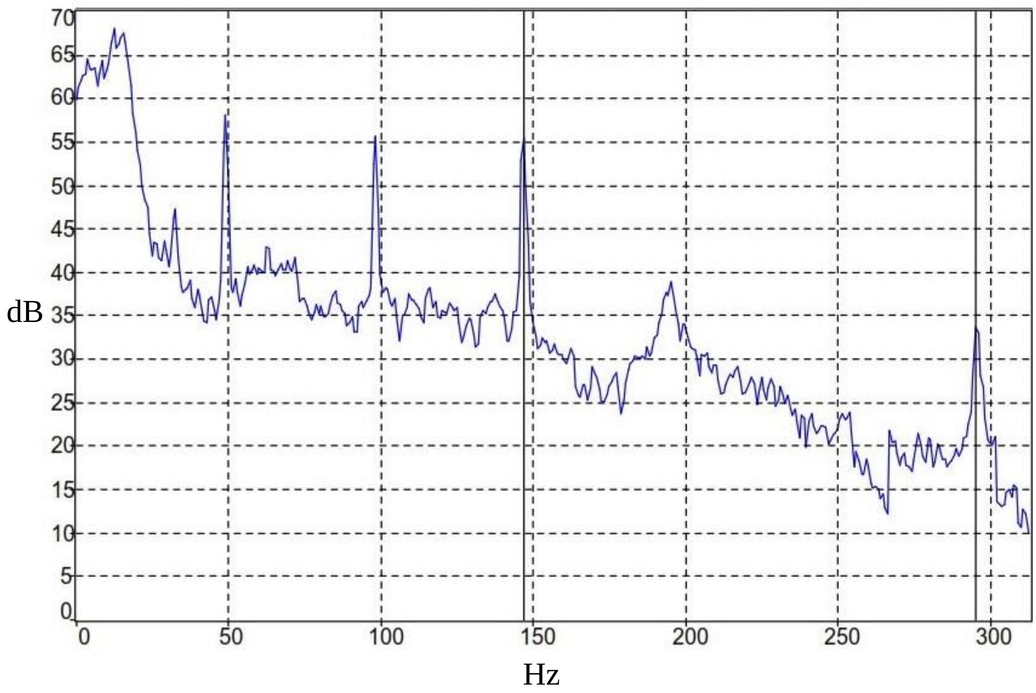

Figure 5.4 : Sound pressure vs frequency spectrum.

Considering these results, if the interaction between the freezer cavity and air duct is investigated at the intervals of 0 – 250 Hz, it can be seen that some natural frequencies shows good agreement with the peak frequencies obtained from the experimental acoustic modal analysis of the freezer cavity. Table 5.4 shows the comparison of the natural frequencies of air duct and the peak frequencies of freezer cavity.

Table 5.4 : The comparison of the frequencies between freezer cavity and air duct.

Peak Frequencies (Hz)	
Freezer Cavity	Air Duct
31.2	32.8 (evap. cover)
56.2	55.5 (fan louver)
65.6	-
87.5	89.8 (evap. cover)
103.1	104.0 (fan louver)
118.7	-
134.3	133.0 (fan louver)
150.0	149.0 (fan louver)
178.1	-
203.1	-

As a conclusion, the blade passing frequency of freezer fan and the 10^{th} normal mode of fan louver are very close to each other. This situation indicate that the freezer fan could excite the fan louver in its nominal working frequency and cause the vibration of the fan louver. These vibrations turn into sound energy which is radiated from the fan louver and increase the amplitude of the sound pressure inside the cavity. This phenomenon really happens because of that one of the resonance frequencies have been seen at the cavity is 150 Hz.

In order to reduce this interaction between the structure and cavity, two methods could be followed; one is the lowering amplitude of the resonance frequency and other is the shifting the resonance frequency.

The first method could be achieved by adding the damping material to the points which have a maximum deformation considering the mode shape of the fan louver at the resonance frequency. But this method is not applicable due to the restrictions related to human health.

The shifting the resonance frequency could be succeed just by some design modification. For this purpose, the rotation speed and the number of blades of the fan could be change to alter the excitation frequency. But all these options also changes the cooling performance of the refrigerator, so this is not a preferred method.

In this study, the structural modification was applied to the fan louver shown in Figure 5.5 since the other methods are not applicable to the refrigerator in reality. The thickness of the fan louver was increased for shifting the natural frequencies of itself. The change in frequencies was observed when the thickness had been increased. The optimum thickness was found as 2.1 mm (the current thickness is 2.0 mm). Table 5.5 shows the natural frequencies of modified fan louver.

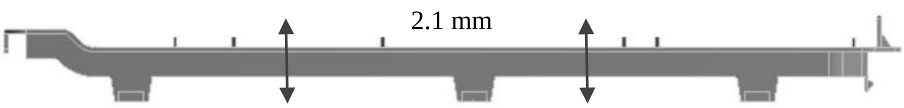

Figure 5.5 : The modified fan louver.

Table 5.5 : The natural frequencies of modified fan louver.

Natural Frequencies (Hz) Numerical Model
5.0
38.3
51.4
57.3
80.1
110.3
116.8
137.1
138.9
157.7

By means of this modification, the 10^{th} normal mode of fan louver was moved up to 157.7 Hz in frequency domain, also none of the sub-modes overlap with the blade passing frequency. Thus the interaction between the structure and cavity was reduced.

6. CONCLUSION AND OUTLOOK

In the frame of this work, acoustic characteristic of the refrigerator freezer compartment is investigated. A reliable and accurate numeric model is developed to simulate the coupled behavior of the structure and acoustic cavity for the freezer compartment. The mixed finite element method is used to solve the acoustic-structure interaction of the acoustic cavity coupled with elastic body. The numerical results show how the coupled structures change the natural frequencies and mode shapes of the acoustic cavity.

The numeric results are validated with the experimental analyses. For this purpose, experimental modal analysis of the fan louver and evaporator cover is performed and the natural frequencies are found respectively. Finally, experimental acoustic modal analysis is implemented to the freezer cavity thus normal modes which belonged to both of the acoustic cavity and coupled structures are obtained.

These results show the normal modes of the fan louver and the evaporator cover change the acoustic characteristic of the freezer compartment, especially in low frequency interval.

Finally, the noise generation mechanism inside the freezer compartment is investigated in normal working conditions of the refrigerator. The resonance frequencies are obtained generated by fan unit. The overlapping frequencies between the source and structures are shifted by some design modifications. Thus the structural borne noise which is radiated from the air duct into the freezer cavity is reduced.

REFERENCES

Akl, W., El-Sabbah, A., Al-Mitani, K., and Baz, A. (2009). Topology optimization of a plate coupled with acoustic cavity. Active and Passive Smart Structures and Integrated Systems. Proc. of SPIE, Vol. 6928, 692811-1.

Baran, M., Bolejko, R., Pruchnicki, P., Zoltogorski, B., and Dobrucki, A. (2009). Refrigerator Noise and Vibration control and Optimization. The Sixteenth International Congress on sound and Vibration, Krakow, 5-9 July.

Bernardi, C., Maday, T., and Patera, A. T. (1994). A new nonconforming approach to domain decompositon: the mortar element method. Nonlinear partial differantial equations and their applications, Pages 13-51.

Bommes, L., Fricke, J., and Klaes, K. (2003). Ventilatoren, Vulkan Verlag, Essen.

Carlsson, H. (1992). Finite element analysis of structure-acoustic systems; formulations and solution strategies. TVSM 1005, Structural Mechanics, LTH, Lund University, Box 118, SE-221 00 Lund, Sweden.

Carolus, T. (2003). Ventilatoren – Aerodynamischer Entwurf, Schallvorhersage, Konstruksion, Teubner Verlag, Wiesbaden.

Fischer, M., and Gaul, L. (2006). Large-Scale Simulations of Acoustic-Structure Interaction Using the Fast Multipole BEM. Acoustic nad Hydro-Acoustic Radiation of Vibrating Structures, Institute of Applied and Experimental Mechanics, Unviersity of Stuttgart.

Gerard, A., Berry, A., and Masson, P. (2005). Control of Tonal Noise from Subsonic Axial Fan. Part 1: Reconstruction of aeroacoustic source from far-field sound pressure, Journal of Sound and Vibration, Vol. 288, No. 4-5, Pages 1049-1075.

Gue, F., Cheong, C., and Kim, T. (2011). Development of Low-Noise Axial Cooling Fans in a Household Refrigerator. Journal of Mechanical Science and Technology, Vol. 25, No. 12, Pages 2995-3004.

Heo, S., Cheong, C., and Kim, T. (2011). Development of Low-Noise Cantrifugal Fans for A Refrigerator Using Inclined S-Shaped Trailing Edge. International Journal of Refrigeration, DOI: 10.1016/j.ijrefrig.2011.07.003.

Igarashi, S., and Kitagawa, K. (2002). Numerical Analysis for Propeller Fan in Freezing Compartment of Household Refrigerator. The 9th of International Symposium on Transport Phenomena and Dynamics of Rotating Machinery, Honolulu, Hawaii, February 10-14.

Jensen, J. S., Yoon, G. H., and Sigmund, O. (2006). Topological design of acoustic-structure interaction structures with the mixed finite element method. III. European Conference on Copmutational Mechanics, Solids, Structures and Coupled Problems in Engineering, Lisbon, Portugal, June 5-8.

Kim, Y., Yang, B., and Kim, C. (2006). Noise Source Identification of Small Fan-BLDC Motor System for Refrigerators. International Journal of Rotating Machinery, Volume 2006, Article ID 63214, Pages 1-7.

Lee, S., Heo, S., and Cheong, C. (2010). Prediction and Reduction of Internal Blade-Passing Frequency Noise of The Centrifugal Fan in Refrigerator. Internal Journal of Refrigeration, Vol. 33, Pages 1129-1141.

Lighthill, M. J. (1952). On Sound Generated Aerodynamically. I. General Theory, Proc. Roy. Soc., Vol. 211A, Pages 564-587.

Maaloum, A., Kouidri, S., and Rey, R. (2004). Aeroacoustic Performance Evaluation of Axial Flow Fans Based on The Unsteady Pressure Field on The Blade Surface. Applied Acoustics, Vol. 65, Pages 367-384.

Maretta, R. M. A., and Tassone, G. (2001). A Vorticity Based Aeroacoustic Prediction for The Noise Emission of A Low-Speed Turbulent Internal Flow, Computers and Fluids, Vol. 32, Pages 457-478.

Mathews, I. C. (1986). Numerical Techniques for Three-Dimensional Steady-State Fluid-Structure Interaction. Journal of Acoustical Society of America, Vol. 79, No. 5, Pages 1317-1325.

Minami, S., Kataoka, S., Kawai, H., Yamada, T., and Yoshimura, S. (2014). A parallel iterative partitioned coupling analysis system for large-scale acoustic fluid-structure interaction. Comput. Mech., Springer-Verlag Berlin Heidelberg.

Neise, W. (1976). Noise Reduction in Centrifugal Fans: A Literature Survey. Journal of Sound and Vibration, Vol. 45, No. 3, Pages 375-403.

Neise, W. (1982). Review of Noise Reduction Methods for Centrifugal Fans. Journal of Engineering for Industry, Vol. 104, Pages 151-161.

Ottosen, N., and Peterson, H. (1992). Introduction to the Finite Element Method. Prentice Hall, New York.

Rajakumar, C., Ali, A., and Yunus, S. M. (1990). A Boundary Element – Finite Element Coupled Acoustic Element for Fluid-Structure Interaction Problems. Boundary Element Methods in Engineering, Springer-Verlag Berlin Heidelberg.

Seo, S., Kwak, T., Kim, C., Park, J., and Jo, K. (2000). Noise and vibration reduction of a household refrigerator. In Proceedings of HVAC Refrigeration Engineering, p. 1133-1140.

Sorgüven, E. (2004). A Computational Aeroacoustics Method Using Large Eddy Simulation and Acoustic Analogy, Phd Thesis, University of Karlsruhe, Germany.

Svanberg, K. (1987). The method of moving asymptotes – a new method for structural optimization. International journal for Numerical Methods in Engineering, Vol. 24, Pages 359-373.

Svanberg, K., (1999). The MMA for modeling and solving optimization problems. Proceedings of the Third World Congress of structural and Multidisiplinary Optimization.

Tajima, H., Miyashita, K., Itou, M., Tamura, A., and Konno, T. (1987). Analysis of Cogging Torque by Finite Element Methods. Transaction of IEEE of Japan, Vol. 107-D, No. 5, Pages 635-641.

Takushima, A., Shinobu, Y., Tanaka, S., Eguchi, M., and Matsuki, K. (1992). Fan Noise Reduction of Household Refrigerator. IEEE Transactions on Industry Applications, Vol. 28, No. 2, March/April.

Velarde-Suarez, S. (2006). Experimental Determination of The Tonal Noise Sources in A Centrifugal Fan. Journal of Sound and Vibration, Vol. 295, Pages 781-796.

Velarde-Suarez, S. (2008). Reduction of The Aerodynamic Tonal Noise of A Forward-Curved Centrifugal Fan by Modification of The Volute Tongue Geometry. Applied Acoustics, Vol. 69, Pages 225-232.

Zienkiewicz, O. C., and Newton, R. E. (1969). Coupled Vibrations of A Structure Submerged in A Compressible Fluid. Proc. Int. Symp. on Finite Element Techniques, Stuttgart, Pages 359-379.

CIRRICULUM VITAE

Name Surname: Onur ÇELİKKAN

Place and Date of Birth: 20.12.1984

Address: İzmir

E-Mail: onur_celikkan@hotmail.com

B.Sc.: Dokuz Eylül University